Turbulence induced by prescribed horizontal heterogeneous water vapor concentrations in a nocturnal stable boundary layer

Master student: Giovanni Negro
1st supervisor: Prof. Stephan de Roode
2nd supervisor: Prof. Aarnout van Delden

March 5, 2021

I, Giovanni Negro, master student of the master program Climate Physics provided by the Utrecht University, am the only author of this work.

Abstract

High resolution simulations of a nocturnal stable boundary layer with initial horizontal heterogeneous water vapor concentrations show three features; the main balancing circulation, internal gravity waves activity and turbulence development. Two regions are found. One, close to the surface, is characterized by high variability of the velocity field, by high values of kinetic, and turbulent kinetic energy and by local breaks of the virtual potential temperature vertical stratification. The second region, above the first one, is characterized by internal gravity waves variability, by low values of kinetic, and turbulent kinetic energies and by a stable virtual potential temperature stratification for all times. Two frequencies are found to be dominant in the system; the lowest is dominant in the surface region, the highest is dominant in the upper region. Both are present in the whole domain.

1 Introduction

"At night under clear skies, radiation to space cools the land surface, which in turn cools the adjacent air through processes of molecular conduction, turbulence, and radiative transfer. This causes a stable boundary layer to form and grow to depths of a few hundreds of meters, depending on the season. Many interacting processes can occur within the statically stable nocturnal boundary layer: patchy sporadic turbulence, internal gravity waves, drainage flows, inertial oscillations, and nocturnal jets" American Meteorology Society

The term - nocturnal boundary layer - is used to address the time evolution problem of the lowest part of the atmosphere during the night. Under specific large scale flow conditions, the nocturnal boundary layer turns out to be stable, leading to the name of Nocturnal Stable Boundary Layer (NSBL). The representation of the NSBL in numerical forecasts and climate models is recognized to be problematic (Cuxart et al., 2006). The complexity arises mainly by the interactions between the different physical processes present in the NSBL: subsidence, horizontal advection, turbulence, and long wave radiation. Various are the works carried over one of these processes or interactions between them.
The following research focuses on a possible *turbulence* production induced by horizontal heterogeneous conditions in the *long wave fluxes*. The literature over these two processes, which had a major impact on the development of the current research, is hereby briefly presented.

Turbulence. Basic stable boundary layer theory, which assumes turbulence to be shear-induced and should apply to the NSBL problem, states that for Richardson numbers $R_i > 0.25$ turbulence will be damped. However, under those conditions, observations show specific humidity transport due to turbulence, close to the surface, and independent of the Richardson number (de Roode, Bosveld, & Kroon, 2010). Even dropping the assumption that turbulent

length scale of momentum and heat are the same, assumption that leads to the existence of said critical Richardson number and holds for neutral and weak stratified boundary layers (Zilitinkevich, Elperin, Kleeorin, & Rogachevskii, 2007), turbulence should still be dumped for increasing stratification, and thus being dependent on the Richardson number.
This contradiction suggests other mechanisms, besides the shear instability, able to produce turbulence in the NSBL. Possible candidates are the buoyancy waves, also known as internal gravity waves (IGW). These waves are able to produce propagating low-magnitude turbulence when small perturbation theory is applicable, or sporadic high-magnitude turbulence, when instability is met (Staquet & Sommeria, 2002). This becomes problematic in turbulent closure models, where no inclusion of such processes is made and thus, turbulence is underestimated (Jacobitz, Rogers, & Ferziger, 2005).

Long wave radiation. Focusing on the heat equation, the work of (Sun et al., 2003), based on night-time observations of the BL, shows that long wave flux divergence and sensible heat flux divergence can have the same contribution in the said equation. In the work (Naumann, Stevens, Hohenegger, & Mellado, 2017), a two columns model of a dry convective boundary layer with different cooling rates, which readily corresponds to horizontal heterogeneous long wave fluxes conditions, it is shown to develop a circulation. The work of (Hohenegger & Stevens, 2016) pictures the same circulation when prescribing horizontal heterogeneous water vapor concentrations in RCE simulations (Radiative Convective Equilibrium). These last two pieces of research confirm that long wave radiation not only influence the heat equation but the momentum equation as well, once that horizontal heterogeneity is met.

The goal of this research is to show that prescribed horizontal heterogeneous concentrations of water vapor, through their influence on the long wave radiation balance, may lead to turbulence production, even in stable NSBL free from large scale forcing. To test this hypothesis, simulations are carried with the help of DALES (Dutch atmosphere Large Eddy Simulation).

The first section focus is on the physics and the knowledge acquired over the Nocturnal Stable Boundary Layer (NSBL). The second section describes the main features of the DALES model. The third section describes the mechanism able to develop a dynamic and derives a useful quantity to estimate the horizontal heterogeneity of the cooling rates, associated with the long wave fluxes horizontal heterogeneity. In the fourth section, the conditions imposed on the simulations are presented. The fifth section is addressed for the results and the discussion. In the last section, the conclusions are drawn.

The exact set of governing equations, in the cloud-free case, with no water phase change and no sources, except the long wave radiative fluxes, is given by:

$$D_t\theta = -\frac{1}{\rho c_p}\vec{\nabla}\cdot\vec{R_{LW}} \tag{1}$$

$$D_t q_v = 0 \tag{2}$$

$$D_t\vec{u} = -\theta_v\vec{\nabla}\Pi - g\hat{k} - 2\vec{\Omega}\times\vec{u} - \nu\nabla^2\vec{u} \tag{3}$$

Of this set, [eq.1] is the governing equation of the potential temperature, [eq.2] is the governing equation of the specific humidity and [eq.3] is the momentum equation. The reader should be familiar with these equations and with the terms composing them. If not, the first two equations are treated in [Section 1.1], the third equation is treated in [Section 1.2]. In [Section 1.3] the transport processes of momentum, heat, and mass are described.

1.1 Scalar fields: θ_v, θ, q_v

Here the virtual potential temperature θ_v is defined, its governing equation derived, and its spatial distribution in the NSBL described. The virtual potential temperature represents the connection between the scalar fields and the dynamic field $\vec{u}$, through the first term on the r.h.s. of [eq.3]. Being θ_v the scalar field ruling the dynamic, it is one of the most important NSBL variables.

Definition

The virtual potential temperature is defined as:

$$\theta_v \equiv T_v\left(\frac{P_{ref}}{P}\right)^{\frac{R}{c_p}} \tag{4}$$

where T_v is the virtual temperature $[K]$, P is the air parcel's pressure $[Pa]$, P_{ref} is a reference pressure, taken here as the pressure at the surface, R is the gas constant for dry air ($= 287.05\ J\ kg^{-1}\ K^{-1}$), and c_p is the thermal capacity at constant pressure for dry air ($= 1005\ J\ kg^{-1}\ K^{-1}$).

The virtual temperature, which follows from the gas law and Dalton's law including water vapor, in the cloud-free case, and with no phase change, is defined as:

$$T_v \equiv T\frac{1+q/\gamma}{1+q} \tag{5}$$

where T is the air parcel temperature $[K]$, q is the water vapor concentration in the air parcel $[kg\ kg^{-1}]$ and $\gamma = 0.622$ is the ratio between the molecular weight of water vapor and the molecular weight of dry air.

Due to the fact that in Earth's atmosphere water vapor concentrations above 0.01 $kg\ kg^{-1}$ are rarely observed, [eq.5] can be expanded around $q \approx 0$ introducing an error $\mathcal{O}(10^{-3}K)$:

$$T_v \approx T(1 + \epsilon q) \tag{6}$$

with $\epsilon \equiv (1-\gamma)/\gamma = 0.608$. Once that the specific humidity q_v, units $[kg\ kg^{-1}]$, is used instead of the water vapor concentration q, [eq.6] is exact.

By means of [eq.6], the virtual potential temperature introduced in [eq.4] can be written as:

$$\theta_v = T\left(\frac{P_{ref}}{P}\right)^{\frac{R}{c_p}}(1 + \epsilon q_v) = \theta(1 + \epsilon q_v) \tag{7}$$

where the definition of potential temperature was used. From now on [eq.7] is addressed, instead of [eq.4], whenever the computation of the virtual potential temperature is required.
From [eq.7], it's clear that the virtual potential temperature is weakly dependent on q_v and strongly dependent on θ. In the limit, $q_v \to 0$, potential temperature and virtual potential temperature coincide. Under this light, θ_v is an estimate of the air parcel's specific entropy, as it was θ in the case free from water vapor. Being the density of an air parcel inversely proportional to its entropy, a positive gradient of θ_v corresponds to a negative gradient of ρ.

Governing equations

The governing equation of θ_v is derived from the governing equations of θ and q_v. After the application of the Reynolds decomposition, [eq.1] and [eq.2] become:

$$D_t\theta = -\frac{1}{\rho c_p}\vec{\nabla} \cdot \vec{R_{LW}} - \partial_i\overline{u_i'\theta'} \tag{8}$$

$$D_t q_v = -\partial_i\overline{u_i' q_v'} \tag{9}$$

where the l.h.s. of the equations are the material derivatives of the two scalar fields. On the r.h.s., the over-lined terms are the statistical description of the turbulent fluxes, expressed using the Einstein notation. Different parametrizations could be applied to these turbulent terms, to quantify the unresolved turbulence (e.g. as it is done in large scale models, where the computational power does not allow high resolution). In [Section 2.2], the parametrization adopted by DALES is shown and explained, even if the starting equations are not Reynolds-decomposed but scale-filtered. In [eq.8], $\vec{R_{LW}}$ is the long wave fluxes field. The long wave radiative fluxes are the ones present in the night time and when their divergence is positive, energy is transported away from the air parcel, marking a decrease in its temperature.
Expanding the divergence, the following can be written:

$$\vec{\nabla} \cdot \vec{R_{LW}} = \partial_x R_{LW\,x} + \partial_y R_{LW\,y} + \partial_z R_{LW\,z} \approx \partial_z R_{LW\,z}$$

where the last passage is based on two considerations. 1) The radiative imbalance is stronger in the vertical direction ($R_{LW\,z} >> R_{LW\,x}$ and $R_{LW\,y}$). 2) The long wave fluxes are dependent on θ and q_v, thus their divergence is also dependent on the gradient of these two scalars. Due to the observed vertical anisotropy of the scalar fields, the horizontal divergence of the long wave fluxes is negligible compared to the vertical divergence, and the total divergence is dropped in favor of the latter one.

The governing equation of the virtual potential temperature, using [eq.7], is then given by:

$$D_t\theta_v = (D_t\theta)(1 + \epsilon q_v) + \theta\epsilon(D_t q_v) \tag{10}$$

Vertical anisotropy

The NSBL presents a major feature in the spatial distribution of θ_v. The absence of short wave radiative fluxes and the positive vertical transport of energy by means of the long wave radiative fluxes allow the formation, under dynamic circumstances imposed by the large scale flow, of a positive vertical gradient $\partial_z\theta_v > 0$, driven by the strong cooling of the ground surface.
The positive vertical stratification of the virtual potential temperature leads to inequality over the vertical profiles of q_v and θ which must be met when a boundary layer is stable:

$$\begin{aligned} \partial_z\theta_v &= \partial_z\theta(1 + \epsilon q_v) + \epsilon\theta\partial_z q_v > 0 \\ \Rightarrow \qquad \partial_z q_v &> -\frac{(1 + \epsilon q_v)}{\epsilon\theta}\partial_z\theta \end{aligned} \tag{11}$$

According to [eq.11], $\partial_z\theta$ can be negative and still have $\partial_z\theta_v > 0$. However, the required positive vertical stratification of q_v would be so large that at the NSBL's top, the values of water vapor concentration will exceed the one observed in Earth's atmosphere. In the NSBL, $\partial_z\theta$ is positive, while the profiles of water vapor concentration fall into fulfilling [eq.11]; both $\partial_z q_v > 0$ and $\partial_z q_v < 0$ profiles are allowed, but the latter are way more common.

Before it was said that θ_v is inversely proportional to ρ. Thus, the requirement $\partial_z\theta_v > 0$ leads to $\partial_z\rho < 0$. Intuitively, increasing the vertical stratification of θ_v increases the stability of the system. This is shown in the next part.

1.2 Dynamic field

In this part, from the equation of motion, it is shown how the positive vertical stratification of θ_v plays a crucial role in the dynamic, ensuring a certain stability. After describing said stability, the mechanisms able to perturb it, readily

the advective instability and the shear instability, are explained.

Equation of motion

With the use of the Boussinesq approximation in the vertical momentum equation, the traditional Coriolis approximation, and the Reynolds decomposition applied, the momentum equation [eq.3] can be written as:

$$Horiz. \begin{cases} D_t u - fv = -\theta_v \partial_x \Pi - \partial_i \overline{u_i' u'} + \nu \nabla^2 u \\ D_t v + fu = -\theta_v \partial_y \Pi - \partial_i \overline{u_i' v'} + \nu \nabla^2 v \end{cases} \tag{12}$$

$$D_t w = -\theta_v \partial_z \Pi + \frac{g}{\overline{\theta_v}}(\theta_v - \overline{\theta_v}) - \partial_i \overline{u_i' w'} + \nu \nabla^2 w \tag{13}$$

where D_t is the material derivative, u, v and w are the components of the resolved flow velocity, f is the Coriolis parameter, equal to $2\Omega \sin \phi$, g is the gravity acceleration, $\overline{\theta_v}$ is the horizontal mean of θ_v at the height considered. The last term of each equation represents molecular diffusion, the over-lined terms represent turbulent fluxes of momentum through the Reynolds decomposition, and Π is the Exner function.

Internal Gravity Waves

According to [eq.13], if an air parcel acquires a virtual potential temperature different than the mean of its level, it acquires a vertical velocity as well. In this case, it is said that the air parcel has acquired a buoyancy because it tends to be displaced by the surrounding air parcels. For a vertically stratified fluid $\partial_z \theta_v > 0$ initially at rest, the dynamic of the small perturbations, which follows from [eq.13], is stable, leading to the name of *stable boundary layer*.
In order to show this, consider an air parcel, at rest at time $t = 0$ in a motionless stable boundary layer $\partial_z \theta_v > 0$, with virtual potential temperature equal to the mean value of its level, $\theta_{parcel} = \overline{\theta_v}$. At time $t = t'$, the air parcel is lifted of δz to a level characterized by a horizontal mean virtual potential temperature $\overline{\theta_v} + \partial_z \theta_v \delta z$. The increment δz should be taken small enough for the perturbation to be considered small, however, there's no strict and unique condition on that. Substituting the parcel's virtual potential temperature, conserved under adiabatic conditions, the background virtual potential temperature of the new level and expressing the vertical velocity as $\partial_t \delta z$, [eq.13] becomes:

$$\partial_{tt} \delta z = -\frac{g \partial_z \theta_v}{\overline{\theta_v}} \delta z \tag{14}$$

which is the differential equation of the harmonic oscillator with frequency:

$$\omega = \pm \sqrt{\frac{g \partial_z \theta_v}{\overline{\theta_v}}} = \pm N \tag{15}$$

called Brunt-Vaisala frequency. In a vertical stratified layer, initially at rest, a parcel, if vertically displaced from its initial position, oscillates around its level of rest, a level defined by having the same virtual potential temperature (slab horizontal mean value) as the air parcel itself. This kind of dynamic, which affects stably stratified fluids, is known by the name of internal gravity waves (IGWs). The Brunt-Vaisala frequency is a good estimate of the NSBL's stratification because it's inversely proportional to the characteristic time of its natural oscillations.

In deriving [eq.14] and [eq.15], only a vertical displacement of the parcel was taken into account. By linearizing all the momentum equations around $\vec{u} = 0$ and assuming an unbound solution in the form $e^{k_x x + k_y y + k_z z - i\omega t}$, the frequency of the IGWs becomes:

$$\omega = N\sqrt{\frac{k_x^2 + k_y^2}{k_x^2 + k_y^2 + k_z^2}} + f\sqrt{\frac{k_z^2}{k_x^2 + k_y^2 + k_z^2}} = N\cos(\alpha) + f\sin(\alpha) \tag{16}$$

where α is the angle between the IGW's propagating vector $\vec{k}$ and the horizontal plane. When the wave propagates horizontally, $\alpha = 0$, [eq.15] is found back. When the wave propagates vertically, $\alpha = \pi/2$, the displacement is horizontal and the parcel does not feel any buoyancy. Still, it is subjected to inertia oscillations.
Through $N >> f$, a condition found in strong stratified layers as the NSBL, the frequencies allowed for the small perturbations are then, from [eq.16]:

$$f^2 < \omega^2 < N_{max}^2 \tag{17}$$

Once that the boundary condition $w_{|z=0} = 0$ is imposed, the linearized equations become a eigenvalue problem with vertical modes, $w \propto \mathcal{W}(z)e^{k_x x + k_y y - i\omega t}$ and $\mathcal{W}(z) = \sin k_z z$. However, the spectrum of k_z is not discrete but continuous, because only one boundary condition is applied.

What was said so far holds in the small perturbation theory. A condition for small perturbation can be cast in the dynamic variables as:

$$U/\omega << 2\pi/\sqrt{k_x^2 + k_y^2} \tag{18}$$

which corresponds to ask the horizontal displacement caused by the wave to be smaller than the horizontal wavelength. Using [eq.16] and neglecting the inertial part, this condition becomes:

$$U << \frac{2\pi N}{\sqrt{k_x^2 + k_y^2 + k_z^2}} \leq \frac{2\pi N}{k_i} = \lambda_i N \tag{19}$$

where λ_i is the wavelength in the x_i direction. When this condition is not fulfilled, the wave may break and become unstable. This is known as *advective*

instability. Note that only the horizontal part of the wave's displacement is taken into account because a vertical displacement preserves the stratification. Readily, horizontally propagating IGWs over a flat surface are stable.

Shear flow

The most recognized physical mechanism able to break the stratification of the NSBL is the shear of the flow, as observed in the work (Newsom & Banta, 2003). This, known as shear produced instability, is way more effective in leading turbulence production, compared with the advection instability cited above. In [Fig.1] a schematic of such mechanism is pictured.

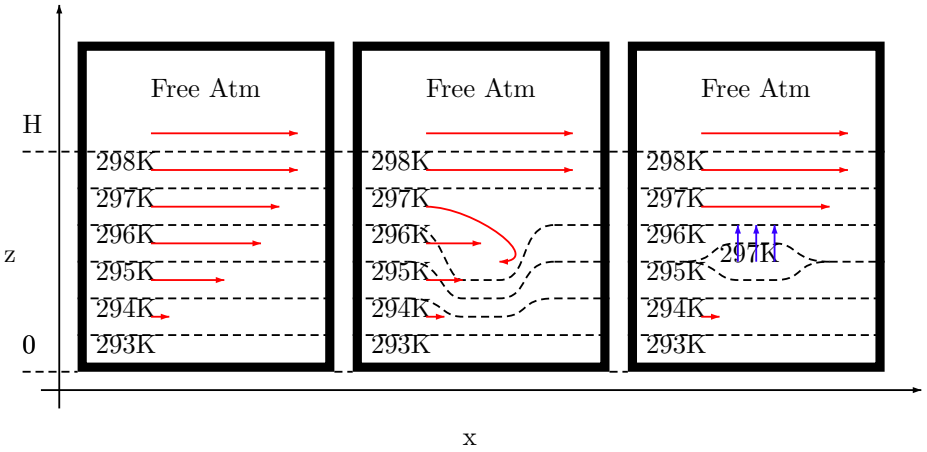

Figure 1: Schematic picture of shear-induced instability in a vertical section of the NSBL. Red arrows (velocities) blue arrows (buoyancy) black dashed lines (isolines of θ_v). From left to right: initial stable state, development of the perturbation, break, and turbulent production. H represents the height of the NSBL, which can vary from few meters up to several hundred meters. Above the NSBL, there is the free troposphere. The stratification of virtual potential temperature is exaggerated, being $1K$ per level.

As initial condition, $w = 0$ everywhere and θ_v is horizontal homogeneous. The large scale flow shears with height due to the no-slip boundary condition at the surface. This leads to a vertical stratification of the horizontal velocities. The kinetic energy may be used to increase the potential energy of the system. At the end of the process, turbulent mixing has happened, lifting the center of gravity of the whole system, while the velocities have decreased.
It's important to highlight that the energy for the mixing is taken from the kinetic energy, while the arise of the instability is only due to the shear of the flow. That means that even energetic flows, but with small values of velocity shear, do not cause mixing in a stratified fluid. On the other hand, low energetic

flows, with shear high enough to make the perturbation unstable, can mix the stratified fluid, even if maybe not completely.

The turbulent shear production follows the Kolmogorov cascade: at some length $l = l_E$ the energy can be moved from the KE stratification to the TKE (turbulent kinetic energy). The TKE is then transported below $l < l_E$ until l_ϵ is met, the length scale at which dissipation takes place. This is not what happens for the IGW instability, where turbulence is produced just in the region where $\lambda = U/N$, marking a sporadic production (Staquet & Sommeria, 2002).

The common condition for assuring a stable shearing flow is given by introducing the Richardson number:

$$R_i = \frac{N^2}{(d\overline{u}/dz)^2} > \frac{1}{4} \tag{20}$$

where N is the Brunt-Vaisala frequency and $\overline{u}$ the horizontal velocity (i.e. $\overline{u}^2 = u^2 + v^2$). This condition follows from the parametrization of turbulence used, in particular from the assumption that the turbulent length scale of momentum and heat are the same. In the work of (Zilitinkevich et al., 2007), it was shown that the existence of such critical Richardson number has no sense once that $l_{TM} \neq l_{TH}$. In these kinds of schemes, turbulent is usually suppressed by increasing stratification, but may as well still develop. This can be an explanation for one of the results found in (de Roode et al., 2010), readily the presence of specific humidity turbulent transport for $R_i > 0.25$. However, in the same work, specific humidity turbulent transport seems to be independent of the Richardson number, while, according to (Zilitinkevich et al., 2007), it can be present, but it should decrease increasing R_i. In other words, the new insight over turbulence given by (Zilitinkevich et al., 2007) explains the observation of turbulence for $R_i > 0.25$ but does not explain its independence by R_i itself.

1.3 Transport processes

In the time evolution of the NSBL, four mechanisms are recognized to be of primary importance: subsidence, horizontal advection, turbulence, and long wave radiation.

Subsidence

Above the BL, the free troposphere is present. It extends from H, the height of the BL, up to ≈ 10 km. This part of the atmosphere is dominated by large scale flow, which can induce subsidence. In presence of a high pressure system in the free troposphere, the horizontal divergence is positive in the BL: cold air is laterally advected and warmer air takes its place while the height of the BL changes (it can increase or decrease, depending on the surface temperature). Subsidence plays a key role in the formation of the NSBL, being positively cor-

related with its stratification (Carlson & Stull, 1986).

Horizontal advection

Due to the high stability of the vertical displacements (i.e. given the vertical anisotropy, small adiabatic vertical displacements are bound to be local), the horizontal dynamic is preferred in stable layers. This is a result of the IWGs activity. A stably stratified fluid, once perturbed, tends to adjust with horizontal transport of the scalar quantities. Convergence and divergence patterns, which match the vertical gradient of the vertical velocity in the continuity equation, arise. Even in the work of (Hohenegger & Stevens, 2016) and of (Naumann et al., 2017), horizontal heterogeneity in cooling rates induces a balancing circulation, which shows high values of horizontal velocity ($1\ m\ s^{-1}$) and vertical velocity $2 \sim 3$ orders smaller. The possibility of horizontal circulations in stratified fluids induced by IGWs was observed for the first time in (Kataoka & Akylas, 2015) and high-lines how IWGs can have a much more important role in the energy budget than thought.

Turbulence

Turbulence is suppressed during the night-time by the formation of the NSBL itself (Ohya, Neff, & Meroney, 1997). However, as it was said, it can develop following an instability and become again of relevance in the transport of scalar and dynamic quantities (Koop & Browand, 1979). Indeed, it is known that during the night, turbulent heat flux divergence can have the same contribution on the heat budget as the radiative long wave flux divergence (André & Mahrt, 1982). So far, the only mechanism widely recognized to lead turbulence production in the NSBL is the shear of the flow. However, it is largely documented (Staquet & Sommeria, 2002) by numerical simulations, lab experiments, and observations, that also internal gravity waves can produce instability and consequentially turbulence, even if they do not follow the Kolmogorov cascade.

Long wave radiation

In the NSBL, the net long wave radiative fluxes (i.e. the sum of the downwards and upwards long wave fluxes) are positive, because the surface is losing energy, transporting it to the free troposphere above. Moreover, the net long wave radiative fluxes increase with height, since the peak of radiation imbalance is found at the top of the NSBL, where the free troposphere is in contact with the colder air of the NSBL. Being the long wave radiative fluxes monotonically increasing with height, their divergence is positive and according to [eq.1] the potential temperature in the NSBL decreases.

A basic model of long wave radiation transport based on Kirchoff's absorption and emission law can be written as:

$$LW_{up}(z) = LW_{up}(z - dz)e^{-\int_{z-dz}^{z} c_u \rho \sigma_A dz} \tag{21}$$

$$LW_{down}(z) = LW_{down}(z + dz)e^{-\int_{z}^{z+dz} c_d \rho \sigma_A dz} \tag{22}$$

where LW_{up} are the upward positive fluxes, LW_{down} are the downward negative fluxes. Then ρ is the air parcel density, function of θ_v, thus weakly q_v-dependent and mostly θ-dependent. The absorber σ_A, in this research, corresponds to q_v. Finally, c_u and c_d are the absorption coefficients for upward and downward radiation.

2 DALES model

In this section, the numerical scheme implemented in DALES (Dutch Atmosphere Large Eddy Simulation) is briefly explained. The simulation resolves the equation of motion and the equation of the scalar fields down to defined scales, constrained by the mesh-size. Below such scales, a SFS-TKE equation (subfilter scale turbulent kinetic energy equation) is implemented. A parametrization of the turbulent fluxes as well as a parametrization of the long wave radiation transfer can then close the NSBL problem.

2.1 Scalar and momentum equations

The scalar and momentum equations, assuming the Boussinesq approximation, applying the LES filter and neglecting molecular transport[1], is given by (Heus et al., 2010):

$$\frac{\partial \widetilde{\varphi}}{\partial t} = -\frac{\partial \widetilde{u_j}\widetilde{\varphi}}{\partial x_j} - \frac{R_{u_j,\varphi}}{\partial x_j} + S_\varphi \tag{23}$$

$$\frac{\partial \widetilde{u_i}}{\partial t} = -\frac{\partial \widetilde{u_i}\widetilde{u_j}}{\partial x_j} - \frac{\partial \pi}{\partial x_i} + \frac{g}{\theta_{v|0}}\widetilde{\theta_v}\delta_{i3} + \mathcal{F}_i - \frac{\partial \tau_{ij}}{\partial x_j} \tag{24}$$

$$\frac{\partial \widetilde{u_i}}{\partial x_i} = 0 \tag{25}$$

where the tildes denote the filtered mean variables. Of this set, [eq.23] is the scalar equation, [eq.24] is the momentum equation and [eq.25] is the continuity equation, introduced assuming incompressibility.

S.E. Scalar Equation [eq.23]

The first term in the r.h.s. represents advection by the mean flow.
The second term in the r.h.s. represents turbulent transport through the divergence of the subfilter-scale (SFS) scalar fluxes, defined as:

$$R_{u_j,\varphi} \equiv \widetilde{u_i\varphi} - \widetilde{u_i}\widetilde{\varphi} \tag{26}$$

The SFS scalar fluxes need a parametrization computed from the filtered mean variables. This will be done in the subsection reserved for the SFS-TKE equation. The third term in the r.h.s. represents the scalar sources.
For the water vapor concentration, the source is set to zero:

$$S_{q_v} = 0 \tag{27}$$

[1]Molecular diffusion is not implemented in DALES. The subfilter diffusion scheme, which is implemented, represents subgrid diffusion due to subgrid turbulence. For the goal of this thesis, diffusion should not play a role in the transport of the scalar and dynamic fields, neither as molecular diffusion neither as subgrid turbulence diffusion. This because molecular diffusion should be negligible compared with turbulence transport and subgrid turbulence diffusion should be negligible compared with the resolved turbulence, given the choices made.

preventing evaporation and condensation events which can release latent heat and lead to vertical motions. Such vertical motions would be induced by phase change and not by long wave radiation horizontal heterogeneity. Ruled by the dew point temperature, such events occur in the real NSBL but are not allowed in this work exactly to fulfill the goal of the thesis and indeed were ruled out starting from the definition of virtual temperature given in [eq.5].
For the potential temperature, the source consists of the vertical divergence of the long wave radiative fluxes, thus:

$$S_\theta = -\frac{1}{\rho c_p}\frac{\partial LW(\vec{x})}{\partial z} \tag{28}$$

M.E. Momentum Equation [eq.24]

The first term in the r.h.s. represents advection by the mean flow.
The second term in the r.h.s. represents the gradient of the pressure, inclusive of the reduced pressure and the trace of the asinotropic SFS-stress tensor τ_{ij}, which will be defined later. The pressure is then given by:

$$\pi = \frac{\widetilde{P}}{\rho} + \sum_i \tau_{ii} \tag{29}$$

The third term in the r.h.s. represents gravity, with $\theta_{v|0}$ being the surface virtual potential temperature and θ_v the virtual potential temperature of the air parcel.
The fourth term in the r.h.s. represents the external forcing terms. In the chase of interest, the only external force allowed is the Coriolis one, thus:

$$\mathcal{F}_i = \mathcal{F}_i^{COR} = -2\epsilon_{ijk}\Omega_j\widetilde{u_k} \tag{30}$$

The last term is the divergence of the asinotropic SFS-stress tensor, defined as:

$$\tau_{ij} \equiv \widetilde{u_i u_j} - \widetilde{u}_i\widetilde{u}_j - \frac{2}{3}\delta_{ij}e \tag{31}$$

The SFS-stress tensor, as well as the SFS scalar fluxes presented in the S.E., need a parametrization, given in [Section 2.2].

C.E. Continuity Equation [eq.25]

The continuity equation, which corresponds to the incompressibility assumption, can be recast by mean of the momentum equation into a prognostic Poisson equation for the pressure π:

$$\frac{\partial^2\pi}{\partial x_i^2} = \frac{\partial}{\partial x_i}\left(-\frac{\partial u_i u_j}{\partial x_j} + \frac{g}{\theta_{v|0}}\theta_v\delta_{i3} + \mathcal{F}_i - \frac{\partial\tau_{ij}}{\partial x_j}\right) \tag{32}$$

The Poisson equation is solved by applying a Fast Fourier Transform in the horizontal directions followed by solving a linear system in the z-direction.

2.2 SFS-TKE equation and parametrization

The subfilter scale model (SFS model) consists of subtracting from the full equations of motion the solution of the filtered mean variables and then, introducing a new variable, casting a new equation. The new variable is the residual turbulent kinetic energy, called subfilter scale turbulent kinetic energy (SFS-TKE), and defined by:

$$e \equiv \sum_{i=1,2,3} \frac{1}{2}(\widetilde{u_i u_i} - \widetilde{u}_i \widetilde{u}_i) \tag{33}$$

and the governing equation for e is found to be:

$$\frac{\partial e}{\partial t} = -\frac{\partial u_i e}{\partial x_i} - \tau_{ij}\frac{\partial u_j}{\partial x_i} + \frac{g}{\theta_{v|0}} R_{w,\theta_v} - \frac{\partial R_{u_i,e}}{\partial x_i} - \frac{1}{\rho_0}\frac{\partial R_{u_i,P}}{\partial x_i} - \epsilon \tag{34}$$

In the r.h.s. of the SFS-TKE equation, the first term is advection of TKE by the mean flow, the second term is shear production due to the shear-instability, the third term is buoyancy production, the fourth term is TKE transport due to turbulence itself, the fifth term is TKE production by pressure fluctuation, the last term is dissipation due to molecular viscosity.

In order to close the SFS-TKE equation in function of the mean filtered variables, a parametrization of $\tau_{ij}, R_{w,\theta_v}, R_{ui,e}, R_{u_i,P}$ and ϵ is needed, as well as a definition of the constants used inside these parametrizations. The parametrizations used in the DALES are the following:

$$\begin{aligned}
\text{II term}: &\quad \tau_{ij} = -K_m(\partial_j u_i + \partial_i u_j) \\
\text{III term}: &\quad R_{w,\theta_v} = -K_H \partial_z \theta_v \\
\text{IV-V term}: &\quad \partial_i(R_{u_i,e} + R_{u_i,P}/\rho_0) = -\partial_i(2K_m \partial_i e) \\
\text{VI term}: &\quad \epsilon = C_\epsilon e^{3/2}/\lambda
\end{aligned}$$

where K_m and K_H are the momentum turbulent diffusion and the heat turbulent diffusion. The parameters are then calculated from the following set:

α	C_f	C_{ϵ_1}	C_{ϵ_2}	C_{h_1}	C_{h_2}	C_N
1.5	2.5	0.19	0.5	1	2	0.76

according to the following equations:

$$
\begin{aligned}
\Delta &= (\Delta x \Delta y \Delta z)^{1/3} \\
\lambda &= \min(\Delta, C_N e^{1/2}/N) \\
C_m &= (C_f/2\pi)(3\alpha/2)^{-3/2} \\
K_m &= C_m \lambda e^{1/2} \\
C_h &= (C_{h_1} + C_{h_2}\lambda/\Delta) C_m \\
K_H &= C_h \lambda e^{1/2} \\
C_\epsilon &= C_{\epsilon_1} + C_{\epsilon_2}\lambda/\Delta
\end{aligned}
$$

With these choices, the SFS-TKE equation is closed in:

$$
\frac{\partial e^{1/2}}{\partial t} = -u_i \frac{\partial e^{1/2}}{\partial x_i} + \frac{1}{2e^{1/2}} \left[K_m \left(\frac{\partial u_i}{\partial x_j} + \frac{\partial u_j}{\partial x_i} \right) \frac{\partial u_j}{x_i} - K_H \frac{g}{\theta_0} \frac{\partial \theta_v}{\partial z} \right] + \\
+ \frac{\partial}{\partial x_i} \left(2K_m \frac{\partial e^{1/2}}{\partial x_i} \right) - \frac{c_\epsilon e}{2\lambda} \tag{35}
$$

The buoyancy term tends to suppress turbulence, being $\partial_z \theta_v > 0$. This is exactly the reason why a decrease in the turbulent kinetic energy is expected (if computed through the parametrization), while increasing the stratification of the system.

2.3 Radiative scheme

In the simulations carried, a full radiation scheme was applied. The full radiation scheme implemented in DALES follows from (Fu & Liou, 1992).

2.4 Nudging terms

In DALES the simulated domain spans from $z = 0$ to $z = H$. The real physical domain, however, merges into the free troposphere continuously. As consequence, the upper part of the simulated domain is affected by the reflection of wave patterns, a reflection that is not observed in the real case NSBL.
In order to overcome such problem, a nudging field $N_F(\vec{x})$ is introduced for each variable of the problem $F \in (\theta, q_v, \vec{v})$ and a nudging term is introduced in each governing equation. The nudging fields are equal to the variables fields at time $t = 0$. The governing equations are then equal to:

$$
D_t F(\vec{x}, t) = ... - \frac{F(\vec{x}, t) - N_F(\vec{x})}{T(z)} \qquad N_F(\vec{x}) = F(\vec{x}, 0) \tag{36}
$$

where F represents the variable, $D_t F(\vec{x}, t) = ...$ the corresponding governing equation (M.E. or S.E.) and the nudging term is given by the difference between the variable's values at time t and its initial value, divided by the characteristic

time $T(z)$. The nudging term tends to restore the initial field of the variable and the magnitude of this tendency is ruled by $1/T(z)$. In the simulations carried, $T(z)$ is prescribed to be $10^{10}s$ for each level in the domain, except for the highest ten levels, where its value, after a rapid drop, reaches $10s$. With such a vertical profile of T(z), the nudging terms are negligible in the bulk of the domain and are dominant in the upper boundary. The top of the NSBL is nudged towards the motionless case, ensuring the dynamic of the bulk to be free from unrealistic reflections.
Reflections usually affect only the upper half of the NSBL so that an eventually dynamic in the lower half cannot be ascribed to them. This can be shown in simulations free from nudging terms, with prescribed heterogeneous q_v in the lowest half of the domain. However, the introduction of nudging terms erases a possible interaction between the upper dynamic and the lower one, representing a more than a valid choice.

It should be pointed out that including non-physical terms in the governing equations has erased a possible dynamic induced by wave reflection at the top, but has made the upper 1/3 of the domain non-physical. In this work, the perturbations are prescribed only in the lower half of the domain, where results can be trusted.

2.5 General remarks

In [Fig.2] a flow chart of the DALES modules is presented. Among them, the following should not be of relevance:

1. Subgrid diffusion: equal to the diffusion due to the subgrid turbulence. The conditions on the simulations are taken for the resolved turbulence to be one order over the subgrid turbulence. Thus, subgrid diffusion should be negligible compared with the resolved diffusion due to the resolved turbulent fluxes.

2. Large scale forcing: ignored in this study because the simulations are initialized as large scale forcing free.

3. Micro-physics: responsible for clouds and liquid water formation, thus can be ignored.

4. Chemistry: can be ignored because there are no other compounds that can react with the water vapor.

A remark has to be done concerning the boundary conditions: the horizontal boundaries are periodic, while the vertical direction is bounded between a fixed surface and a nudging cap. Moreover, DALES makes use of the Arakawa C-grid: pressure and scalars fields are calculated at the cell-center, the three velocity components on the face of the cell. The level of the cell center is called *full level*, the level where w is computed *half level*.

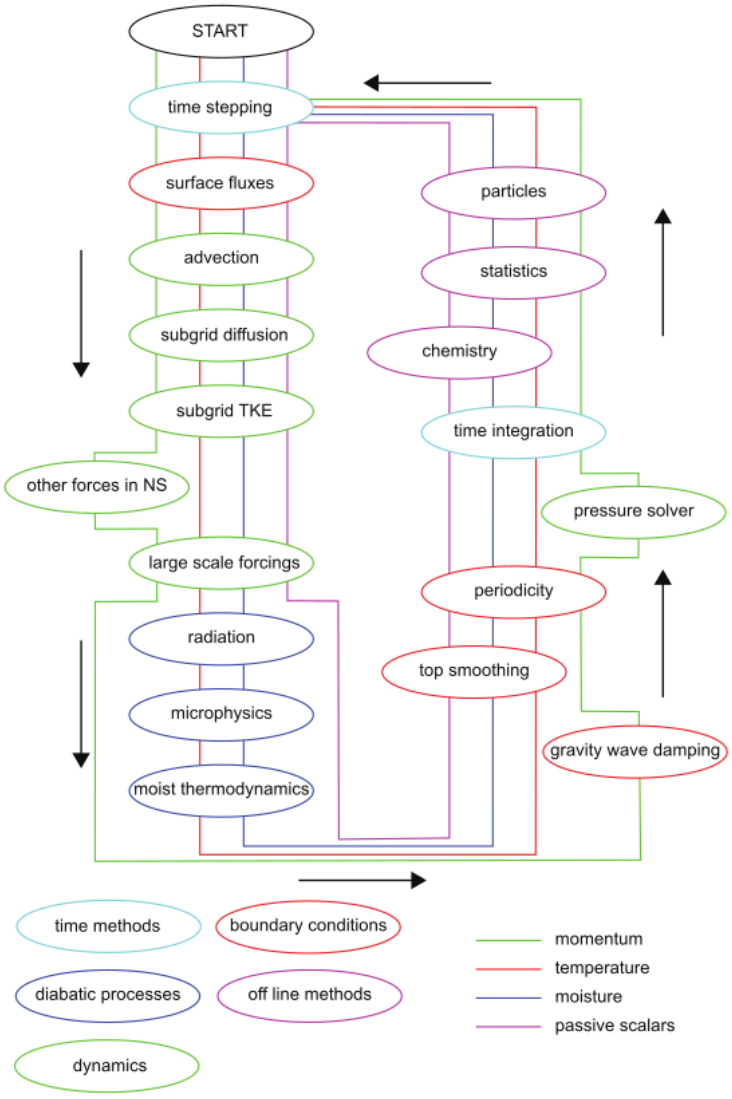

Figure 2: Flow chart of DALES modules, credits to (Heus et al., 2010).

3 Mechanism description

This section shows a mechanism that is recognized to being able to sustain a shallow circulation in the NSBL, even if it is initialized motionless and free from large-scale forcing. Credits for the discovery of such circulation go to (Hohenegger & Stevens, 2016) and for a bulk model of it to (Naumann et al., 2017).

Variables interaction

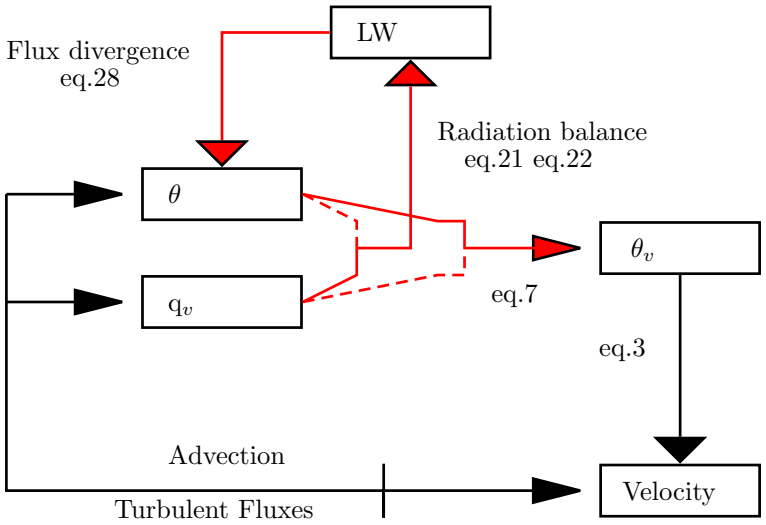

Figure 3: Schematic picture of the interactions among the variables, for a nocturnal stable boundary layer. The red arrows describe the interactions in the motionless state. The black arrows, together with the red ones, describe the interactions once that dynamic develops. The dotted arrows represent a lack of dependency: θ_v is determined mainly by θ, the long wave balance is determined mainly by q_v. Advection and turbulent fluxes affect both the scalars and the dynamic fields.

In [Fig.3], a schematic view of the interactions among the variables is given. Each arrow represents a governing equation, a single term of an equation, or a definition, among the ones presented in [Section 1].

- The spatial distribution of the scalar fields q_v and θ determines the long wave radiation balance of the NSBL [eq.21]&[eq.22].
- The vertical divergence of the long wave fluxes is a source in the θ governing equation [eq.28].

- The scalar fields of q_v and θ, through the definition of θ_v [eq.7] and the momentum equation [eq.3], affect the velocities.
- Advection and turbulent transport redistribute the scalar fields, as well as the dynamic ones. Advection can be distinguished from turbulence by a time window mean where the mean flow corresponds to advection and the fluctuations of the velocity field with respect to the mean to turbulence.
- Turbulence can be divided into low magnitude turbulence, responsible for fluctuations of the velocity field and unable to destroy the vertical θ_v stratification, and high magnitude turbulence, driven by buoyancy following a local break of the vertical θ_v stratification. The stratification break is a sign of instability.

It's clear that if $q_v(\vec{x}) = q_v(z)$ and $\theta(\vec{x}) = \theta(z)$, then $\theta_v(\vec{x}) = \theta_v(z)$ and $LW(\vec{x}) = LW(z)$ follow. Under horizontal homogeneous conditions, the long wave radiative cooling rates are horizontal homogeneous and, in the dynamic equation, the term $(\theta_v - \overline{\theta_v})$ is zero for all times and all points in space. The NSBL evolves decreasing its temperature, but a dynamic does not develop.

Horizontal heterogeneous conditions

Once horizontal heterogeneous water vapor concentrations are applied, the long wave radiation will be horizontal heterogeneous as well. As result, in the horizontal plane, there will be areas characterized by stronger cooling rates and areas characterized by weaker cooling rates. The radiative imbalance results in torque in the vertical plane, which should lead to a dynamic and thus at least to low magnitude turbulence. To show this, let's consider a motionless NSBL with horizontal isoline of virtual potential temperature at $t = 0$ ($\partial_{x,y}\theta_v = 0$) and with horizontal heterogeneity in the long wave fluxes divergence. How to initialize such NSBL is a topic of [Section 4]. Being close to the motionless case allows substituting the material derivative D_t with ∂_t. The governing equations of θ_v and w are then, from [eq.10] and [eq.13]:

$$\partial_t \theta_v = \partial_t \theta(1 + \epsilon q_v) = -\frac{1}{\rho c_p} \partial_z LW(1 + \epsilon q_v) = f(\vec{x})$$

$$\partial_t w = \frac{g}{\overline{\theta_v}}(\theta_v - \overline{\theta_v})$$

Deriving the vertical momentum equation for connecting the two:

$$\partial_t \partial_t w = \frac{g}{\overline{\theta_v}}(\partial_t \theta_v - \partial_t \overline{\theta_v}) - \frac{g}{\overline{\theta_v}^2}(\theta_v - \overline{\theta_v})\partial_t \overline{\theta_v}$$

The last term can be neglected, due to $(\theta_v - \overline{\theta_v})/\overline{\theta_v} << 1$. The commutative properties of the partial derivative and the horizontal mean allows writing:

$$\partial_t \partial_t w = \frac{g}{\overline{\theta_v}}(f(\vec{x}) - \overline{f(\vec{x})})$$

After integrating alongside the horizontal direction:

$$\partial_t \int_0^x \partial_t w dx = \int_0^x \frac{g}{\overline{\theta_v}} (f(\vec{x}) - \overline{f(\vec{x})}) dx \tag{37}$$

The l.h.s. of [eq.37] represents the time derivative of the vertical torque in vertical plane xz. The r.h.s. represents the horizontal heterogeneity of the long wave fluxes divergence in the x direction. Given an area of stronger cooling ($f(\vec{x}) < \overline{f(\vec{x})} < 0$) the system's respond is to decrease the vertical torque.
In [eq.37] the r.h.s. seems a perfect candidate to estimate the horizontal heterogeneity of the long wave flux divergence, being in connection with the time derivative of the vertical torque. However, being the torque a pseudovector, it is better to estimate the heterogeneity as:

$$HH = \int_0^L dx \int_0^L dy \int_0^H \frac{g}{\overline{\theta_v}} |f(\vec{x}) - \overline{f(\vec{x})}| dz \tag{38}$$

Increasing the horizontal heterogeneity it is expected an increase of the energy in the system, being the energy development positive correlated with the vertical torque and the torque positive correlated with the horizontal heterogeneity defined here.

Shallow circulation: $L \approx 100\ km$

Once horizontal heterogeneous concentrations of water vapor are imposed, a shallow circulation can be sustained in the NSBL with $H \approx 600\ m$ and $L \approx 100\ km$. The q_v horizontal heterogeneous spatial distribution affects the long wave radiation fluxes divergence and the horizontal heterogeneous conditions needed for the torque mechanism are met.
In the article (Hohenegger & Stevens, 2016), the circulation is shown to develop in convective boundary layers (i.e. $\partial_z \theta_v \approx 0$). Then, in the article (Naumann et al., 2017), a two columns model with different cooling rates is used to sustain a similar circulation.

The main differences between the cited researches and the current one are the following:

1. This study investigates a stable boundary layer and not a convective boundary layer.

2. This study does not prescribe different cooling rates, but different water vapor concentrations. In other words, the dynamic has a feedback on the scalar fields and thus on the distribution of the cooling rates.

3. The goal of this study is not the circulation by itself, but the turbulent production.

Resolving turbulence: $L \approx 100m$

In the NSBL, turbulence develops on the scale of meters. Thus, to resolve turbulence and keep the integration time feasible, the horizontal domain size has to decrease compared with the works of (Hohenegger & Stevens, 2016) and (Naumann et al., 2017). In particular, willing to keep the number of grid points below two hundred in the horizontal direction, the new horizontal scale of the problem cannot exceed 500 m. This is an important difference with the works cited because it means a drastic increase in the aspect ratio of the problem and, by consequence, a different solution.

4 Conditions on the simulations

Hereby, the conditions imposed on the simulations are described and explained. These conditions follow from the goal of the thesis, which is showing that turbulence in the NSBL is possible even when the shear of the flow is considerably small compared with the stratification ($R_i >> 1$). The arise of turbulence is then achieved solely through horizontal heterogeneous water vapor concentrations. Horizontal heterogeneous water vapor concentrations are imposed at $t = 0$. The section is divided into three parts.

1. The first part treats general conditions imposed on the simulations, as the domain size and the initial velocity field.

2. The second part treats the conditions imposed on the amplitude of the water vapor perturbation.

3. The third part discusses the choice of the spatial distribution of the water vapor perturbation.

4.1 General conditions

Simulation size
The domain has horizontal size $L = 300\ m$ and vertical size $H = 318.75\ m$, resulting in an aspect ratio close to one. A total number of grid points equal to $128 \times 128 \times 128$ is used. The resulting resolution is $2.34m \times 2.34m \times 2.5m$. With this grid size, turbulence is mainly resolved. The total integration time of the simulations is 5 h and the single integration time step is $60s$. Such an integration time step should be able to resolve IGWs, given the stratifications used in the simulations.

Dynamic field
The velocity field inside the NSBL, as well as any large scale dynamic, is initialized as $\vec{v}_{|t=0} = 0 \quad \forall \vec{x} \in D$. The motionless case and the absence of large scale forcing ensure the production of turbulence to not be due to a preexisting dynamic, neither forced by the state of the atmosphere. Ultimately, turbulence is produced by shear or advective instability, but the dynamic or the conditions responsible for that have to develop alongside the simulation and not being imposed.
The Coriolis force is present and the latitude at which the simulations are carried is $\phi = 65°$. However, even if the effects of the Coriolis force are visible with the right analysis, they have a minor impact on the simulations and are not relevant for the turbulent production, especially considering the horizontal domain size used in the simulations.

Free troposphere radiation
Using a full radiation scheme, values of temperature and specific humidity (or other absorbers) are needed even above the NSBL. These values are responsible

for the radiation balance above the NSBL, which has a feedback on the radiation balance of the NSBL. A file is provided to DALES with the temperature and specific humidity values at fixed pressure levels, from the surface up to the top of the atmosphere. While the values of temperature and specific humidity are taken as constant in the pressure levels belonging to the stratosphere ($P < 300hPa \Rightarrow T = 200\ K$, $q_v = 0.0\ kg\ kg^{-1}$), in the pressure levels belonging to the troposphere a vertical profile has to be imposed. For the temperature, it was chosen a linearly decreasing profile, from the value imposed at the NSBL's top to the value of 200 K imposed at the bottom of the stratosphere. For the specific humidity, an exponential decreasing profile was chosen, matching the values of specific humidity imposed at the NSBL's top and at the bottom of the stratosphere.

4.2 Prescribed water vapor concentration

In the simulations carried, horizontal heterogeneous specific humidity values are prescribed at $t = 0$. Then, the system is allowed to evolve without further conditions, except for the nudging terms described in [Section 2.4].

Scalar fields : θ_v, θ, q_v

At $t = 0$ the domain has to be IGWs free (i.e. the virtual potential temperature should not present anomalies in the horizontal plane, with respect to its horizontal mean). Having a small anomaly of virtual potential temperature at the initial state should not be a problem, due to the stability of the system (the solutions are locally bounded if the anomaly is small). However, it's not trivial to choose how small the anomaly of θ_v should be to fall in the definition of small perturbation. To bypass such a problem, the domain is initialized as IGWs free, which corresponds to ask horizontal homogeneity in the virtual potential temperature field: $\theta_v(\vec{x})_{|t=0} = \theta_v(z)$. On the other hand, the q_v scalar field at $t = 0$ must be horizontal heterogeneous, which is in contradiction with the requirement of a horizontal homogeneous field of θ_v, except if a horizontal heterogeneous field of θ is introduced as well, to compensate the q_v heterogeneity.

The simplest way to proceed is using horizontal homogeneous background fields:

$$\begin{aligned} q_B = \overline{c} + q_B(z) \qquad \theta_B = \theta_{surf} + \theta_B(z) \\ \Rightarrow \theta_v(z) = \theta_B(1 + \epsilon q_B) \end{aligned} \tag{39}$$

with $\partial_z \theta_v(z) > 0$. In this work, $\partial_z \theta_B = \overline{c_1} > 0$ is firstly selected, representative of the vertical homogeneous stratification. The horizontal homogeneous background field θ_B is then computed by up-integrating the surface temperature. The profile q_B is computed similarly, selecting $\partial_z q_B = \overline{c_2}$ which fulfills [eq.11]. Then, $\theta_v = \theta_v(z)$ is computed and $\partial_z \theta_v(z) > 0$ is guaranteed.

Over the horizontal homogeneous background fields, horizontal heterogeneity is introduced as a perturbation in the scalar fields of q_v and θ. The two perturbations efface each other, composing the background horizontal homogeneous field $\theta_v(z)$, IGWs free at $t = 0$:

$$[\theta_B + \theta' f_1(\vec{x})][1 + \epsilon(q_B + q'_v f_1(\vec{x}))] = \theta_v(z) = \theta_B(1 + \epsilon q_B) \tag{40}$$

where $\theta_B + \theta' f_1(\vec{x})$ is the initial potential temperature field, $q_B + q'_v f_1(\vec{x})$ is the initial water vapor field, θ' and q'_v are the magnitudes of the heterogeneous perturbations and $f_1(\vec{x})$ is the shape of the perturbations. Of course, the shape of the q_v perturbation and the shape of the θ perturbation has to be the same, and they are discussed later.

Solving [eq.40], the relation between the amplitude of the q_v perturbation and the amplitude of the θ perturbation, relation which guarantees $\theta_v(z)$ at $t = 0$, is found:

$$\theta'_p = -\frac{\epsilon\theta_B}{1 + \epsilon[q_B + q'_v f_1(\vec{x})]} q'_v \tag{41}$$

Once that a heterogeneous field of q_v is prescribed, the corresponding heterogeneous field of θ, which ensures $\partial_{x,y}\theta_v = 0$, is calculated, and those fields represent the initial conditions imposed on the scalar fields. In [Fig 4] are pictured the initial conditions for the three fields in the case of a sine perturbation acting on two levels. Due to the horizontal periodic boundary conditions implemented in DALES, the perturbation at $x = 0$ has to coincide with the perturbation at $x = L$. The same applies to the meridional direction.

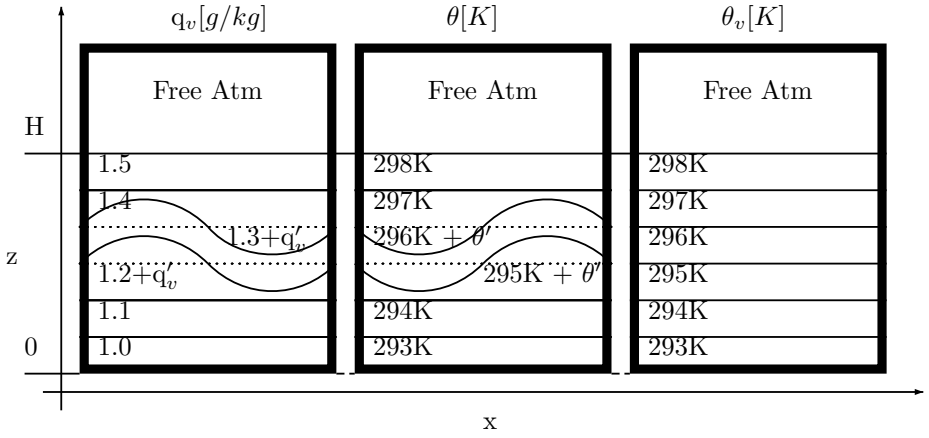

Figure 4: Schematic picture of the initial, prescribed, scalar fields. The background fields are dotted lines, the total fields are continuous lines. The initial background field of θ_v always coincides with the initial total field, ensuring IGWs free conditions at $t = 0$. The values of the vertical gradients are only for explanatory purposes.

It's important to point out that the easing effect of the perturbations $q'_v f_1(\vec{x})$ and $\theta' f_1(\vec{x})$ on each other is just under the dynamical point of view. Being the radiative equations, readily the long wave fluxes and their vertical divergence, differently dependent on θ and q_v, the effect on the cooling rates is not eased at all. At time $t = t'$ the long wave flux divergence has modified $\theta(\vec{x})$, but not $q_v(\vec{x})$, moving $\theta_v(z)$ to $\theta_v(\vec{x})$ and allowing dynamic development.

4.3 Perturbation shape

The perturbation shape $f_1(\vec{x})$ in [eq.40] and [eq.41] can be written as $f_1(\vec{x}) = L(x, y)H(Z)$. As horizontal shape, a Gaussian function was chosen:

$$L(x, y) = e^{-\frac{(x-L/2)^2+(y-L/2)^2}{\sigma^2}} \tag{42}$$

This function respects the open horizontal boundaries conditions. The horizontal heterogeneity is introduced in both the x and y direction, to have a three-dimensional problem and not a two dimensional one. This request follows from the work of (Kataoka & Akylas, 2015); an IGW circulation is possible only when two horizontal directions are taken into account and when the variables change alongside both directions. The Gaussian matches this request as well and put the maximum of the perturbation in the center of the simulation $(x, y) = (L/2, L/2)$.

For what concerns the vertical structure, several things have to be taken into account. Firstly, the presence of nudging terms in the upper part of the system suggests that it's better to apply the perturbation only in the lower half of the domain. That said, H(z) has to drop to zero after $lv = 60$; a vertical gradient of water vapor concentration is introduced as well. To smooth such gradient, a capping is applied to the perturbation. Moreover, the perturbation is attached to the surface. The physical meaning behind this is that horizontal heterogeneity should be forced from a source at the surface. The vertical profile of the perturbation is then chosen, following such requests, as:

$$\begin{aligned} H(z) &= 1 && 0m < z < 125m \\ H(z) &= (150 - z)/25 && 125m < z < 150m \\ H(z) &= 0 && 150m < z < H \end{aligned}$$

In [Fig.5], vertical and horizontal sections of the specific humidity field at time zero are provided. The horizontal extension of the perturbation, quantified by σ, is taken equal to $150m$.

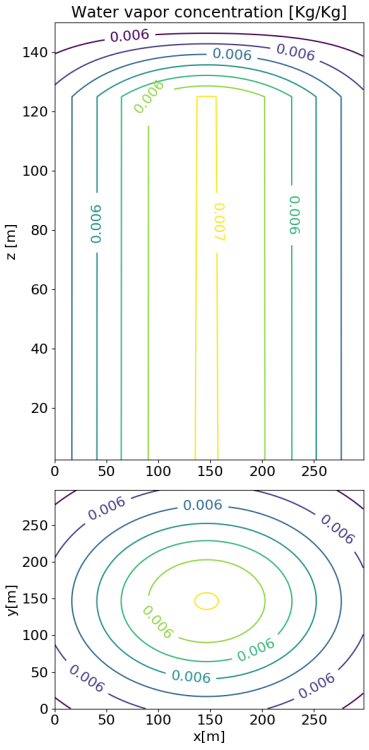

Figure 5: In the top, a vertical section across $y = L/2$ of the water vapor concentration at $t = 0$. In the bottom, a horizontal section across $z = 10\ m$ of the water vapor concentration at $t = 0$. The vertical capping is a linear decrease that matches continuously the scalar fields above. The background, vertical and horizontal homogeneous field q_B was fixed to 6 $g\ kg^{-1}$. The amplitude of the perturbation was fixed to 1 $g\ kg^{-1}$. The horizontal extension of the perturbation, quantified by σ, is fixed to 150 m. Golden isolines correspond to maximum values of q_v, blue isolines to minimum values of q_v.

5 Results and discussion

The results are divided into five parts. Each part treats a different aspect of the problem. In each part, a discussion is provided at the end.

1. The first part focus on the dependencies between the cooling rates vertical profiles and the horizontal homogeneous background fields θ_B and q_B. Simulations with initial horizontal homogeneous conditions are carried. The variables of interest are the surface temperature, the vertical gradient of the potential temperature, the mean value of the specific humidity, and the vertical gradient of the specific humidity. Within this part, a first insight into the problem is given.

2. The second part takes back the definition of horizontal heterogeneity (HH) given in [eq.38] and computes this quantity in simulations with initial horizontal heterogeneous conditions. Varying the perturbation amplitude and the background scalar fields, the dependencies of the horizontal heterogeneity on these quantities is found. Through these dependencies, the key variables of the problem are identified, readily the perturbation amplitude and the virtual potential temperature stratification.

3. The third part pictures the dynamic development, comprehensive of an induced circulation, of internal gravity waves and a turbulence insurgence close to the surface, associated with a local break of the stratification. The time series of the kinetic energy is studied varying the values of stratification and perturbation amplitude. The HH time series is computed as well. A linear correlation analysis is applied between the time derivative of the kinetic energy and the HH time series, to assess if there's a relation at later times (HH is derived from equations holding at $t = 0$).

4. The fourth part focus on turbulence. Vertical profiles of turbulent fluxes of virtual potential temperature suggest the presence of two regions. In the bulk of the NSBL, low magnitude turbulent fluxes can be associated with internal gravity wave activity under stable conditions. At the surface, high magnitude turbulent fluxes can be associated with a local break of the stability. Such instability cannot be ascribed to the shear of the main flow and could be a sign of advective instability or a sign of a bad implementation of the surface conditions.

5. In the last part, a Fourier analysis is applied over the time series of the vertical velocity field, to assess the nature of the wave signals. These are found to be internal gravity waves. Through the associated theory, an insight into the propagating directions can be drawn. According to this insight, horizontally propagating IGWs are dominant in the bulk of the system, while slanted propagating IGWs are dominant at the surface, below $z = 50m$. This may be the reason behind the surface instability.

5.1 The variability of the cooling rates vertical profiles on the horizontal homogeneous background scalar fields

In this set of simulations, the amplitude of the perturbation is set to zero. The goal is to understand the variability of the cooling rates vertical profiles varying the background horizontal homogeneous scalar fields of potential temperature θ_B and specific humidity q_B.

Specific humidity background field : $q_B = \overline{c} + q_B(z)$.

The controlling variables on the background horizontal homogeneous scalar field q_B are the mean value $\overline{c}$ and the vertical gradient $\partial_z q_B(z)$. The latter is chosen for simplicity to be constant. The mean value $\overline{c}$, in a Netherlands-like climate, can span between 2 $g\ kg^{-1}$ up to 10 $g\ kg^{-1}$. With a surface temperature of $T_{surf} = 293\ K$ and a surface pressure of $P_{surf} = 1\ atm$, this range corresponds to relative humidity values between 10% and 70%. Above such range, condensation events occur, forbidden by the goal of this work. The vertical gradient of the specific humidity, as shown in [eq.11], can either be positive or negative, without affecting the stability of the system. Negative values are however more observed.

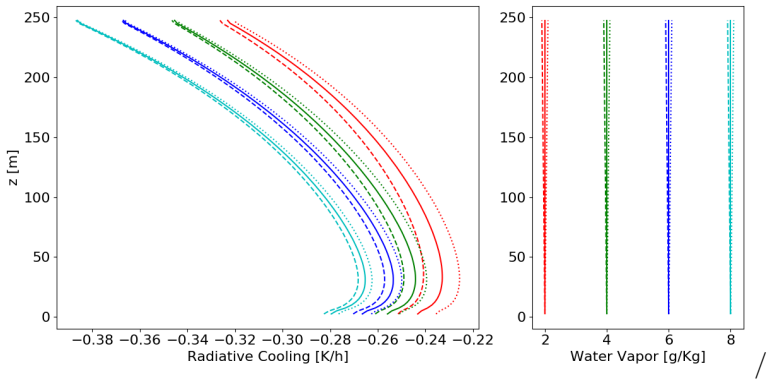

Figure 6: [Left] Cooling rates vertical profiles for different values of $\overline{c}$ and $\partial_z q_B(z)$. [Right] Vertical profiles of q_B. The same color and line type are representative of the same simulation. In this set of simulations, $\theta_{|z=0} = 293\ K$ and $\partial_z \theta_B = 4 \cdot 10^{-3}\ K\ m^{-1}$ were chosen.

In [Fig.6], cooling rates vertical profiles are confronted for different mean values and different vertical gradient signs of the specific humidity background field q_B (negative gradient $= -4 \cdot 10^{-4}\ g\ kg^{-1} m^{-1}$, neutral gradient $= 0\ g\ kg^{-1} m^{-1}$ and positive gradient $= 4 \cdot 10^{-4}\ g\ kg^{-1} m^{-1}$). **[1]** Simulations with higher values of mean specific humidity $\overline{c}$ present smaller cooling rates[2]. **[2]** The vertical

[2]Here it is for the best to fix some notation. Considering the cooling rates as negative,

shape of the cooling rates vertical profiles does not depend strongly on $\overline{c}$ (i.e. increasing the mean specific humidity content of the system, the vertical profile of the cooling rates is shifted to the left, but its profile is preserved). **[3]** The magnitude of the cooling rates is close to being linearly dependent on $\overline{c}$. **[4]** A positive/negative vertical gradient of the specific humidity leads to higher/lower cooling rates in the NSBL. **[5]** The vertical gradient of the specific humidity can have the same influence, on the vertical cooling rates profiles, as the mean value of the specific humidity $\overline{c}$. For instance, below $z = 50m$, the cooling rates associated with the dashed red line and the cooling rates associated with the continuous green line, are close to being equal. **[6]** The same specific humidity vertical gradient loses its influence on the vertical cooling rates profiles increasing the mean value $\overline{c}$: the cooling rates vertical profiles in the chase $\overline{c} = 8\ g\ kg^{-1}$ are almost unaffected by the variation of the vertical gradient of specific humidity.

The last point can be due to the difference in specific humidity between the NSBL top and the NSBL surface, a difference which becomes more and more negligible compared to $\overline{c}$, if the vertical gradient of specific humidity is fixed. To show this is the case, the vertical gradients of specific humidity have to be correlated with the mean values of specific humidity.

In [Fig.7], cooling rates vertical profiles are confronted for different mean values and different vertical gradients of the background specific humidity field. The values of the specific humidity vertical gradient are now negative and correlated with the specific humidity mean values, marking respectively a 10%, 5% and 2.5% deficit of water vapor content at the system's top compared to the system's surface. **[7]** Once that the specific humidity vertical gradients are correlated with the specific humidity mean values, the dependencies of the cooling rates vertical profiles on the specific humidity vertical gradients are again similar for different $\overline{c}$. **[8]** The difference in the cooling rates vertical profiles, between the cases $\partial_z q_B = 0$ and $\partial_z q_B = -\chi\overline{c}$, where χ is the deficit constant, increases for increasing $\overline{c}$.

Potential temperature background field : $\theta_B = \theta_{surf} + \theta_B(z)$.

The potential temperature background field is taken to be function of the surface temperature and the vertical stratification. In [Fig.8] the dependencies of the cooling rates vertical profiles on these two variables is given in the range $T_{surf} = [283\ K, 288\ K, 293\ K]$ and $\partial_z\theta_B(z) = [4 \cdot 10^{-3}\ K\ m^{-1}, 8 \cdot 10^{-3}\ K\ m^{-1}, 12 \cdot 10^{-3}\ K\ m^{-1}]$. **[9]** The cooling rates vertical profiles are similar for different surface temperatures. **[10]** The cooling rates magnitude looks linearly dependent on the surface temperature. **[11]** Increasing/decreasing the stratification leads to a surface increase/decrease of the cooling rates and a

when talking about higher cooling rates or cooling rates increase, it is meant a decrease of their absolute magnitude.

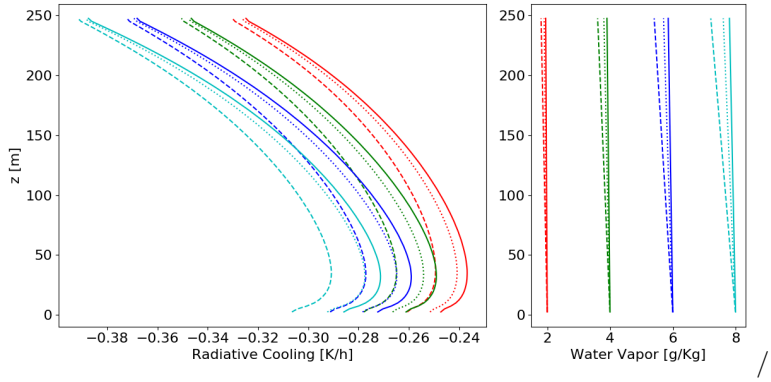

Figure 7: [Left] Cooling rates vertical profiles for different values of $\overline{c}$ and $\partial_z q_B(z)$. [Right] Vertical profiles of q_B. The vertical gradients of specific humidity are now correlated with the mean values of specific humidity. The dashed lines are representative of a 10% deficit, dotted lines of a 5% deficit, continuous lines of a 2.5% deficit of the specific humidity value at the top of the NSBL compared with the surface. The same color and line type are representative of the same simulation. In this set of simulations $\theta_{|z=0} = 293\ K$ and $\partial_z \theta_B = 4 \cdot 10^{-3}\ K\ m^{-1}$ were chosen.

decrease/increase of them at the NSBL top. **[12]** The influence of different stratifications on the cooling rates vertical profiles is similar for different surface temperature. **[13]** Increasing the stratification above $8 \cdot 10^{-3}\ K\ m^{-1}$, the typical NSBL cooling rates vertical profile, which presents a peak of cooling at certain height, is lost.

Discussion

- Through **[1]**, smaller cooling rates are expected in the area where the positive perturbation $q_v' > 0$ is at its peak $(x_0, y_0 = L/2, L/2)$. Air parcels in this column should present downward motion.
- Results **[2][3]** suggest the problem to be independent from the choice of $\overline{c}$. Indeed, it's the horizontal difference of the cooling rates which rules the dynamic development, and not the mean cooling rate. If the differences in the cooling rates between the column where $q_v = \overline{c}$ and the column where $q_v = \overline{c} + q_v'$, varying $\overline{c}$, are independent by the choice of $\overline{c}$ (3) and if this holds in the levels where the perturbation is defined (2), then the horizontal heterogeneity of the cooling rates should be independent by $\overline{c}$.
- For what concerns the vertical gradient of the background specific humidity field, result **[4]** clarifies the capping properties of the absorber on the system. Long wave radiation divergence increases, increasing the water vapor content, and thus it is maximum at the top of the domain if a positive vertical gradient of specific humidity is present. As result, also the downward long wave fluxes

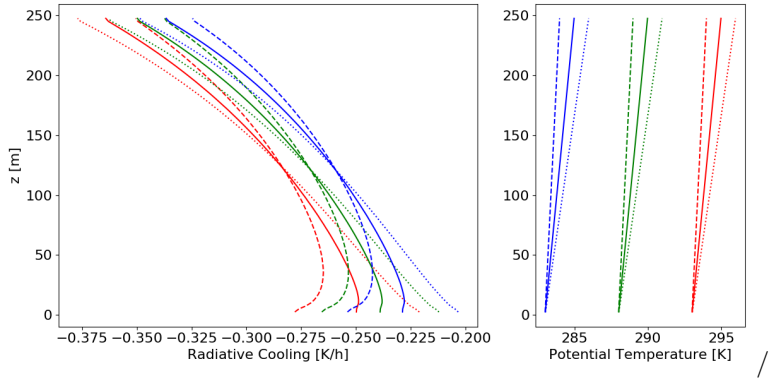

Figure 8: [Left] Cooling rates vertical profiles for different values of θ_{surf} and $\partial_z \theta_B(z)$. [Right] Vertical profiles of θ_B. The same color and line type are representative of the same simulation. In this set of simulations, $\overline{c} = 4\ g\ kg^{-1}$ and $\partial_z q_B(z) = -1.6 \cdot 10^{-3}\ g\ kg^{-1}\ m^{-1}$ were chosen.

increase, marking an increase in the cooling rates below the capping.
- The perturbation described in [Section 4.3] introduces a negative vertical gradient on the water vapor content (the capping between $z = 100m$ and $z = 125m$). In other words, the perturbation marks a decrease of the cooling rates, in both the aspects of water vapor content and water vapor vertical gradient, according to [4]. Result **[5]** shows that this contribution can have the same influence on the cooling rates as q'_v.
- The perturbation was defined as $q'_v f(\vec{x})$ where f is the unitary function (i.e. $max(f) = 1$) with a Gaussian horizontal distribution, a homogeneous vertical distribution and a vertical capping between $z = 100m$ and $z = 125m$. Thus, fixed the perturbation amplitude q'_v also the vertical gradient of the perturbation is fixed (i.e. $q'_v \partial_z f(\vec{x})$). Both $q'_v > 0$ and $q'_v \partial_z f(\vec{x}) < 0$ tend to decrease the cooling rates of the perturbed column. Even if the first contribution (the contribution given by $q'_v > 0$) is independent by the choice of $\overline{c}$ [2-3], the second contribution (the one given by $q'_v \partial_z f(\vec{x})$) decreases its influence increasing $\overline{c}$, according to **[6]**. For this reason, a decrease of the cooling rates horizontal heterogeneity is expected increasing $\overline{c}$, once that $q'_v > 0$ is introduced.
- While confronting different background vertical gradients of specific humidity, result **[7]** suggests it is better to correlate them with the mean values of specific humidity.
- Even so, **[8]** shows there's still a certain variability connected with the vertical gradient of the background specific humidity field.

- Results **[9]**[**10**] are similar to what was seen in [2][3] and the same conclusion can be drawn: the horizontal heterogeneity of the cooling rates should not be strongly dependent on the surface temperature. The explanation for the increase of the cooling rates, decreasing the surface temperature, resides in the positive

long wave transport of energy between the NSBL and the free troposphere, transport that is ruled by the difference in energy between these two systems: if the NSBL is colder than less energy is emitted and the cooling rates increase.
- Increasing the stratification of potential temperature, at fixed surface temperature, means increasing the energy in the upper part of the domain. For this reason, the long wave fluxes divergence will increase there, transporting energy to the free troposphere as well as downward. The downward part is responsible for the increase of the cooling rates in the lower part [**11**]. The inversion (i.e. the height at which the cooling rates are unaffected by the stratification variations) occurs roughly at half the domain's height because a constant vertical gradient of potential temperature is prescribed.
- Result [**12**] suggests that the horizontal heterogeneity should not depend at all on the potential temperature field.
- Due to [**13**] the window of variation for the stratification will be, from now on, $\partial_z \theta_B \in [2 \cdot 10^{-3}\ K\ m^{-1} : 8 \cdot 10^{-3}\ K\ m^{-1}]$.

The horizontal heterogeneity of the cooling rates is dependent on all the variables treated here (close to linear does not mean linear). However, with the results shown so far, the dependencies of the horizontal heterogeneity of the cooling rates on θ_B, compared with the dependencies of the horizontal heterogeneity of the cooling rates on q_B, should be negligible, at least in the ranges shown. In the next section, this will be checked.

5.2 The variability of HH against the horizontal homogeneous background scalar fields and the perturbation amplitude

The variable introduced in [eq.38] can be used to quantify the horizontal heterogeneity of the cooling rates. This variable will be addressed as HH. Firstly, it should be understood under which parameters HH is most dependent, among the following: the background field q_B, the background field θ_B and the perturbation amplitude q_v'. Some insight into these dependencies was already drawn in the previous section. Here, for securing this knowledge, simulations with initial horizontal heterogeneous conditions are carried varying the background scalar fields and the perturbation amplitude. The HH of different simulations, computed at $t = 0$, is then confronted to understand which variables most affect the horizontal heterogeneity of the cooling rates. The variables which have a minor impact on HH will not be varied in the full simulations spanning five hours.
This section is divided into three parts, where HH is confronted varying q_B, θ_B, and q_v'. The hope is for variables like T_{surf} to be of secondary influence on the horizontal heterogeneity of the cooling rates, as it seems from [Section 5.1]. Being the horizontal heterogeneity triggered by $q_v' > 0$, it is most likely that this will be the stronger dependency. However, it is important to quantify the variation of HH while varying the background fields as well.

Specific humidity background field : $q_B = \overline{c} + q_B(z)$

In [Fig.9] the HH's dependencies on the specific humidity background field are shown. **[1]** Comparing the top and bottom figure, $\approx 10\%$ of the horizontal heterogeneity is found above the levels where the perturbation q'_v is applied. **[2]** The horizontal heterogeneity decreases for increasing $\overline{c}$. **[3]** The range of variability of HH, varying $\overline{c}$ and $\partial_z q_B$, decreases increasing $\overline{c}$.

Potential temperature background field : $\theta = \theta_{surf} + \theta_B(z)$

In [Fig.10] the HH's dependencies on the potential temperature background field are shown. **[4]** The variability of HH in the range $T_{surf} \in [288\ K, 293\ K, 298\ K]$ and $\partial_z \theta_B \in [2\ mK\ m^{-1}, 4\ mK\ m^{-1}, 6\ mK\ m^{-1}, 8\ mK\ m^{-1}]$ is smaller that the one computed varying the background field of specific humidity.

Water vapor perturbation amplitude : q'_v

In [Fig.11] the dependencies of HH on q'_v and on $\partial_z \theta_B$ are shown. **[5]** Confronting [Fig.9], [Fig.10] and [Fig.11], it can be concluded that the horizontal heterogeneity of the cooling rates is mainly function of the perturbation[3] amplitude. **[6]** The HH is linearly dependent on the perturbation amplitude. **[7]** The variability of HH connected to the potential temperature stratification increases for increasing perturbation amplitude.

Discussion

- The water vapor perturbation, even if confined in $z \in [0, 125m]$, modifies the vertical profiles of the cooling rates for $z > 125m$. However, the horizontal heterogeneity of the cooling rates found above the perturbation is negligible compared with the one found in the perturbation **[1]**. Dynamic development triggered by horizontal heterogeneous cooling rates should be present both in $z < 125m$ and $z > 125m$, but in the latter region, the forcing (i.e. the horizontal heterogeneity of the cooling rates) is one order smaller.
- The HH's increase for decreasing water vapor mean-content, high-lined in **[2]**, is probably due to the negative vertical gradient of specific humidity introduced with the perturbation and function of the perturbation amplitude. As said in [Section 5.1], the negative vertical gradient of the specific humidity perturbation has a positive feedback on the horizontal heterogeneity of the cooling rates. However, the feedback decreases, increasing the mean specific humidity value, explaining the decrease of HH for increasing mean specific humidity values.
- Due to **[3]**, it is convenient to run simulations in the range $\overline{c} \in [4 : 8] g\ kg^{-1}$. In this range, the variability of HH, and thus the variability of the forcing, is

[3] There are two perturbations, one in the specific humidity field and one in the potential temperature field. However they are bond by a relation which guarantees $\partial_{x,y}\theta_v = 0$ at $t = 0$, and thus it can be addressed as one perturbation.

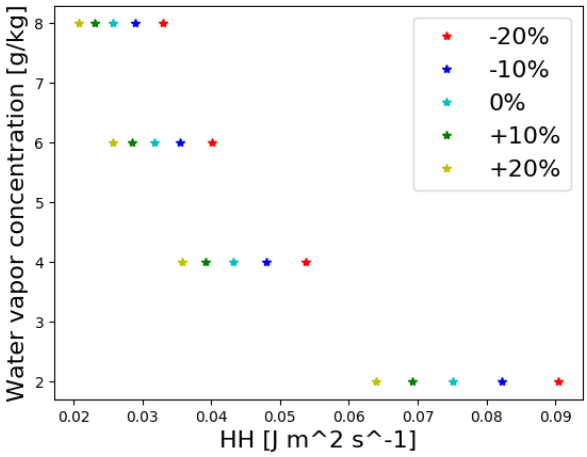

(a) Integrating up to 125m

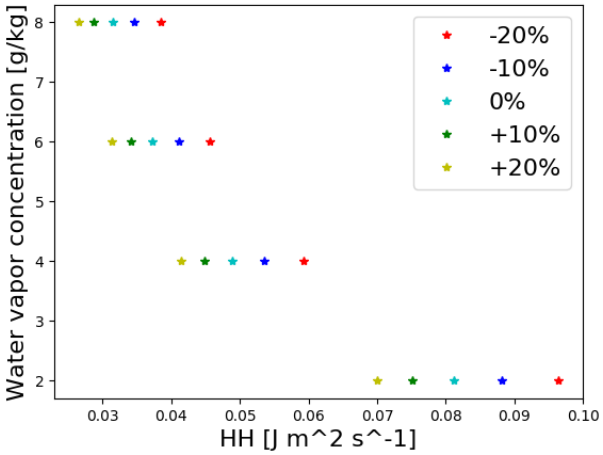

(b) Integrating up to 318.75m

Figure 9: HH's dependencies on $\bar{c}$ and $\partial_z q_B$. On the horizontal axis HH, on the vertical axis $\bar{c}$. Different colors represent different water vapor vertical gradients ($\partial_z q_B$), correlated with the mean values and marking a -20%, -10%, 0%, $+10\%$, $+20\%$ difference between the specific humidity values at the top and at the surface. On top, HH was computed integrating up to the top of the perturbation. Below, HH was computed integrating up to the top of the domain. In all simulations, $\theta_{surf} = 293\ K$, $\partial_z \theta_B = 4\ mK\ m^{-1}$ and $q_v' = 0.5\ g\ kg^{-1}$.

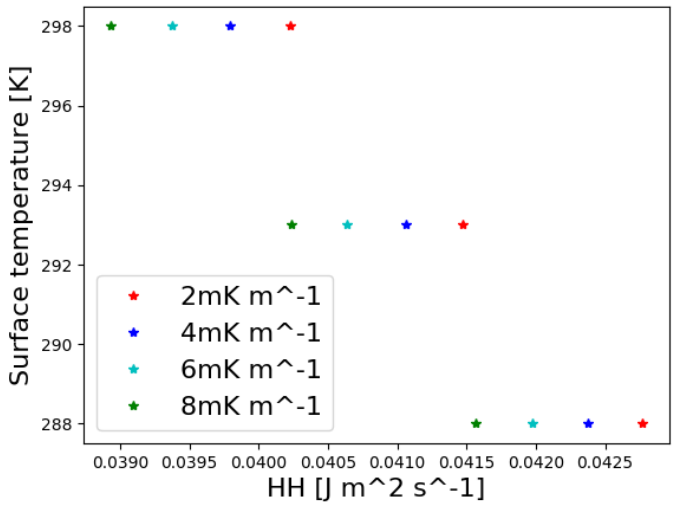

Figure 10: HH's dependencies on T_{surf} and $\partial_z \theta_B$. On the horizontal axis HH, on the vertical axis T_{surf}. Different colors represent different potential temperature vertical gradients ($\partial_z \theta_B$). In all simulations, $\overline{c} = 6\ g\ kg^{-1}$, $\partial_z q_B = -2.4 \cdot 10^{-3}\ g\ kg^{-1}\ m^{-1}$ and $q_v' = 0.5\ g\ kg^{-1}$.

smaller.

- Result **[4]** follows form the similarity between the cooling rates vertical profiles shown in [Section 5.1] when T_{surf} and $\partial_z \theta_B$ are varied. The same level of similarity was not found while confronting cooling rates vertical profiles varying q_B. This suggests that the potential temperature field plays a secondary role in deciding the horizontal heterogeneity of the cooling rates. Simulation varying T_{surf} can be dropped. Indeed the response of the dynamic should not be dependent on the surface temperature and the surface temperature does not play a considerable role in deciding the horizontal heterogeneity of the cooling rates (i.e. it does not play a role either in the forcing, either in the dynamic response). On the other hand, $\partial_z \theta_B$ does not affect considerably HH but has a great influence on the dynamic response of the system. Thus, simulation varying $\partial_z \theta_B$ will be kept.

- Result **[5]** confirms that the insight over the problem given in [Section 5.1] was correct. The horizontal heterogeneity is mainly dependent on the perturbation amplitude and the other fields play a secondary role. For controlling the horizontal heterogeneity of the cooling rates, varying q_v' should be enough, and the other contributions can be neglected.
- Result **[6]** follows from the linear dependence of the cooling rates on $\overline{c}$, pictured

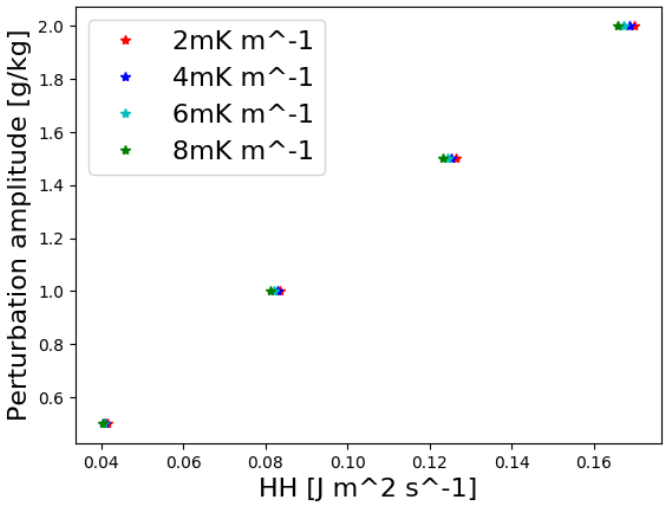

Figure 11: HH's dependencies on q_v' and $\partial_z \theta_B$. On the horizontal axis HH, on the vertical axis q_v'. Different colors represent different potential temperature vertical gradients ($\partial_z \theta_B$). In all simulations, $\overline{c} = 6\ g\ kg^{-1}$, $\partial_z q_B = -2.4 \cdot 10^{-3}\ g\ kg^{-1}\ m^{-1}$ and $T_{surf} = 293K$.

in [Section 5.1].
- Result **[7]** suggests to keep the amplitude of the perturbation below 1 $g\ kg^{-1}$. Higher perturbation amplitudes result in a higher variability connected with the potential temperature stratification and are even more unrealistic[4].

Collecting the results seen so far, it can be concluded that the horizontal heterogeneity of the cooling rates is decided mainly by the amplitude of the perturbation q_v'. On the other hand, it is known that the dynamic development is strongly affected by the vertical stratification of potential temperature. Thus, the main parameters against which the dynamic development should be studied are q_v' and $\partial_z \theta_v$. The other parameters can be taken as constants: $\theta_{surf} = 293\ K$, $\overline{c} = 4\ g\ kg^{-1}$, $\partial_z q_B = -1.6 \cdot 10^{-3}\ g\ kg^{-1}\ m^{-1}$.

5.3 Dynamic and energy development

In this section, the time evolution of simulations with horizontal heterogeneous specific humidity values is described and confronted by varying the key parameters. As result of [Section 5.2], the key parameters are q_v' and $\partial_z \theta_B$. The first

[4] An amplitude of $q_v' = 0.5\ g\ kg^{-1}$ in the specific humidity field is connected with an amplitude of $\theta' = 0.1\ K$ in the potential temperature field. The relation between the two amplitudes can be taken as linear.

one affects the horizontal heterogeneity of the cooling rates (i.e. the forcing), the second one affects the dynamic response.
This section is divided into two parts. In the first part, a picture of the dynamic development is provided, showing the main circulation, IGWs patterns, and high variability of the velocity field at the surface. Then, in the second part, the time evolution of the total kinetic energy in the system is computed and confronted for different values of q'_v and different values of $\partial_z \theta_B$. The time evolution of the variable HH is computed as well. Two important questions will be answered: how the kinetic energy development is dependent on q'_v and $\partial_z \theta_B$ and if the variable introduced in [eq.38] is indeed correlated with the time derivative of the kinetic energy.

Dynamic evolution

In order to give a picture of the dynamic evolution, explanatory results of a simulation are shown. The initial conditions on the simulation are the followings: $T_{surf} = 293\ K$, $\partial_z \theta_B = 4\ mK\ m^{-1}$, $\bar{c} = 4\ g\ kg^{-1}$, $\partial_z q_B = -1.6 \cdot 10^{-3}\ g\ kg^{-1}\ m^{-1}$ and $q'_v = 0.5\ g\ kg^{-1}$.
The dynamic evolution shows the formation of the main circulation, the insurgence of wave-like signals, which reassemble internal gravity waves, and the presence, after $t \approx 30min$, of high variability of the velocity field at the surface, associated with a local break of the stratification. To separate the different processes, a reanalysis is needed.

1. To picture the main circulation at time $t = \bar{t}$, a time mean in the window $[\bar{t} - 15min : \bar{t} + 15min]$ is applied. Such a time window can rule out the high variability of the velocity field at the surface ($T < 5min$) as well as the majority of the IGWs allowed in the system. Horizontally propagating IGWs have a characteristic period of $T = 2\pi N^{-1} \approx 10min$, leaving out from the time mean waves propagating with an angle $\alpha > 60°$. Such an approach does not take into account the variability of the main circulation, which is increasing its magnitude in time. However, the shape of the main circulation should be preserved. In [Fig.12] a picture of the lower part of the main circulation is given.

2. To picture the IGW dynamic at time $t = \bar{t}$, a time mean in the window $[\bar{t} - 5min : \bar{t} + 5min]$ is applied and then is de-trended from the main circulation subtracting the latter. Such a time window should rule out the high variability at the surface ($T < 5min$) and preserve the variability connected to some IGWs (the ones with larger period). Of course, such a reanalysis is not able to give a reliable picture of the IGWs and it is used only for explanatory purposes. A better understanding of the wave activity can be given through turbulence reanalysis [Section 5.4] or the Fourier transform of the velocity field [Section 5.5]. In [Fig.13] an explanatory picture of the IGWs dynamic is given.

3. The surface velocity field's high variability, induced by local breaks of the vertical stratification, overtakes, at $t \approx 30min$, the visibility of the main circu-

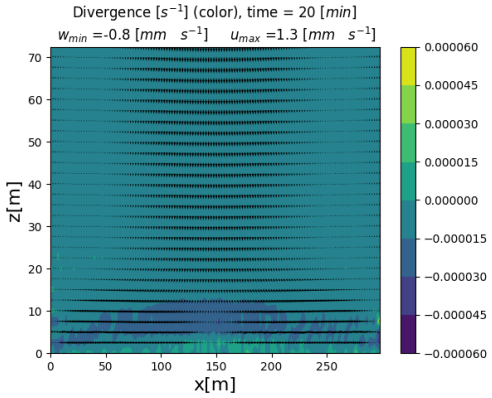

Figure 12: Reanalysis of the velocity field. Vertical section across $y = L/2$ showing the lower half of the mean circulation. Colors represent divergence in the vertical plane, defined as $\partial_x u + \partial_z w$. The maximum vertical velocity is almost half of the maximum horizontal velocity.

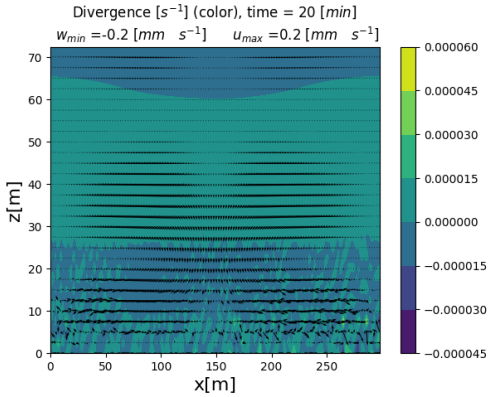

Figure 13: Reanalysis of the velocity field. Vertical section across $y = L/2$ showing the lower half of the IGW dynamics. Colors represent divergence in the vertical plane, defined as $\partial_x u + \partial_z w$. The maximum vertical and horizontal velocities are equals.

lation, and the visibility of the IGWs there (even if the time-means are applied). The high variability makes it impossible to picture these two processes (at least close to the surface) and is the reason why the picture of the main circulation and the wave-like signals is taken at $t = 20min$. The surface velocity field's high variability is described in the corresponding section [Section 5.4].

Energy evolution

The following table assets the conditions on the simulations carried. The other, fixed, background conditions are $\overline{c} = 4\ g\ kg^{-1}$, $\partial_z q_B = -1.6\ g\ kg^{-1}\ m^{-1}$ and $T_{surf} = 293\ K$; these should play a secondary role in the dynamic evolution.

		$\partial_z \theta_B$	
		$4\ mK\ m^{-1}$	$8\ mK\ m^{-1}$
q'_v	$0.5\ g\ kg^{-1}$	S1	S2
	$1.0\ g\ kg^{-1}$	S3	S4

Table 1: The four simulations differ for the stratification and the amplitude of the specific humidity perturbation.

We divided the study of the kinetic energy development in three regions: surface kinetic energy development ($z \in [0m : 25m]$), bulk kinetic energy development ($z \in [25m : 125m]$) and other kinetic energy development ($z \in [125m : 250m]$). The reasons for the separation are two: the high variability and magnitude of the velocity field at the surface after $t \approx 30min$, the vertical extension of the perturbation. To obtain the energies of the three regions, kinetic energy is computed in each grid-cell $KE_{ijk} = \frac{1}{2}(u_{ijk}^2 + v_{ijk}^2 + w_{ijk}^2)$, where [i,j,k] is the grid-point, and then mean in the levels between the heights selected. Thus, it represents the mean kinetic energy per unit of mass and grid-cell.

In [Fig.14] the kinetic energy development in the three regions is shown for the whole integration time. **[1]** From the kinetic energy magnitudes found in the three regions, it's clear that the most energetic is the one close to the surface, at least for $t > 1h$. **[2]** Around this time, a sudden increase of the kinetic energy is seen. **[3]** The surface kinetic energy is the first to increase, followed by the bulk kinetic energy and later by the kinetic energy found above the perturbation. **[4]** The sudden increase in the kinetic energy seems to happen earlier if the perturbation magnitude is increased (green and cyan lines). **[5]** The magnitude of the kinetic energy at the latest times looks independent from the initial conditions.

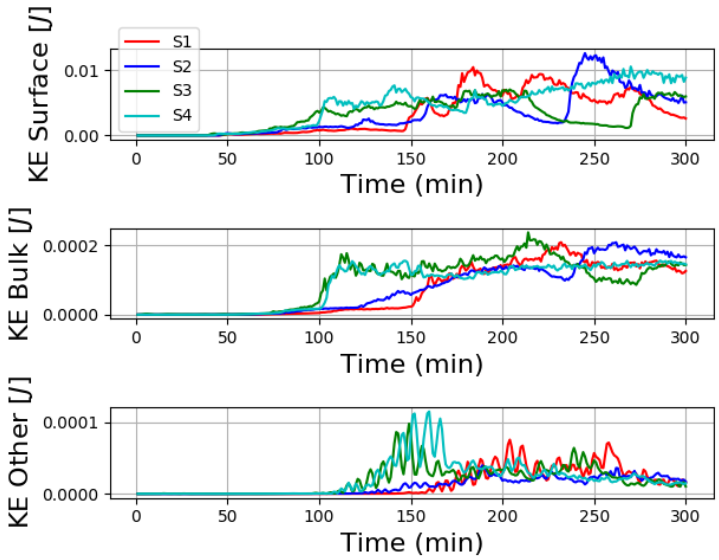

Figure 14: Kinetic energy development per unit of mass and grid-cell in the three regions and for the whole integration time. Energies of 10^{-2} J are associated with a velocity magnitude of 0.1 $m\ s^{-1}$.

To assess the knowledge on the initial kinetic energy development, which is several orders smaller compared with the latest one, [Fig.15] shows the same

results of [Fig.14] but in the first half-hour of the simulations. **[6]** The magnitude of the kinetic energy at the surface and in the bulk are almost the same with the bulk kinetic energy being slightly higher. The kinetic energy of the upper part is one-fourth of the kinetic energy found below. **[7]** At the earliest times, stratification suppresses dynamic development; simulations under higher stratification conditions present lower levels of kinetic energy. **[8]** Increasing the stratification increases the frequency of the kinetic energy variations. **[9]** Doubling the perturbation amplitude increases the kinetic energy of one order.

Lastly, the time series of HH is correlated with the time derivative of the kinetic energy in the three regions and in the first hour, to see if the variable HH is indeed correlated with the time derivative of the kinetic energy, as it seems from its definition. The correlation parameters are shown in [Fig.16]. **[10]** The correlation parameters between $\partial_t KE(t)$ and $H(t)$ are always significant at the surface. **[11]** The correlation parameters between $\partial_t KE(t)$ and $H(t)$ show no correlation in the region above the perturbation. **[12]** The correlation parameters between $\partial_t KE(t)$ and $H(t)$, in the bulk, are non-significant in the low-stratification simulations (S1-S3) and are significant in the high-stratification simulations (S2-S4).

Discussion

Main circulation. The main circulation behaves as expected: in the center of the domain, where the perturbation is at its peak, the air parcels sink due to the stronger cooling rates acting on them. The shape of the circulation is the same as pictured in (Naumann et al., 2017) and (Hohenegger & Stevens, 2016): a main flow at the surface and a returning flow at the top of the perturbation ($H = 125m$, not shown in [Fig.12]). However, the discrepancy in the velocity magnitudes, between our work and the ones cited above, is considerable (three orders). This can be due to different reasons:

- Integration time. In the work of (Naumann et al., 2017) a flow velocity of 1 $m\ s^{-1}$ is found after 2 days of integration when the equilibrium state is reached. The existence of an equilibrium state follows from prescribing cooling rates. This work prescribes water vapor concentrations, which are advected by the dynamic and lose their horizontal heterogeneity (i.e. the equilibrium state is the motionless one). For $t > 20\ min$, the magnitude of the velocities increases, but the insurgence of the surface velocity field's high variability makes it impossible to picture the main circulation below $50m$. In (Naumann et al., 2017) such velocity field high variability is not found because it's a two columns model that does not implement turbulence. In (Hohenegger & Stevens, 2016) the velocity field high variability is not found for the large grid size used ($\approx 7\ km$).

- Domain size. The torque mechanism increases its effectiveness by increasing the horizontal scale of the problem. In the work of (Hohenegger & Stevens, 2016) the horizontal scale is 200 km. In (Naumann et al., 2017)

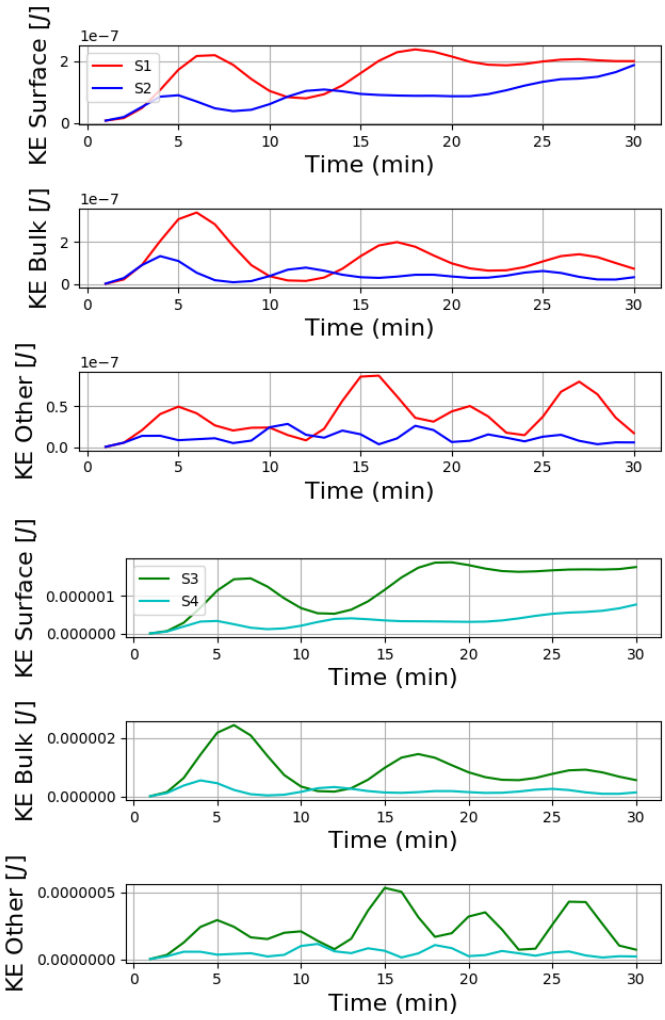

Figure 15: Kinetic energy development in the first half-hour. The different magnitudes of the kinetic energy per unit of mass and grid-cell required two plots. In the upper plot the KE development is confronted for two different stratifications and $q_v' = 0.5\ g\ kg^{-1}$. In the lower plot the KE development is confronted for two different stratifications and $q_v' = 1.0\ g\ kg^{-1}$.

the distance between the two columns is 100 km. Thus, the difference in the horizontal extension between this work and the ones cited is of three orders.

- Cooling rates. The difference in the cooling rates between the two columns in the work of (Naumann et al., 2017) is 1 $K\ hour^{-1}$. In the current

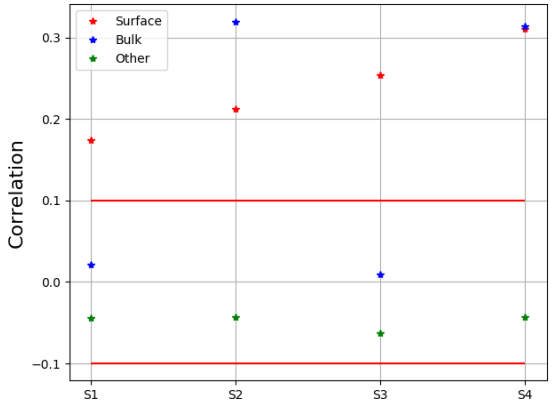

Figure 16: Correlation parameters between HH(t) and ∂_tKE(t) for different simulations and different regions. The time series used for the correlation analysis span the first hour. The correlations parameters are the non-diagonal elements of the covariance matrix computed through the function numpy.cov() implemented in the python libraries. Time series with correlation parameters between the two red lines are considered not correlated.

work, the horizontal variation of the cooling rates is three order smaller [Section 5.1]. However, the horizontal extension of the domain is three orders smaller as well, as said in the previous point. Thus, the horizontal heterogeneity of the cooling rates should be in the same order, meaning that this point and the previous one should be the least suspected reasons for the discrepancy.

- Stratification. Both (Hohenegger & Stevens, 2016) and (Naumann et al., 2017) did not prescribe a stratified layer, but a convective one. The equilibrium height of an air parcel subjected to a stronger cooling rate, compared with the surroundings, in a convective BL is $z = 0$, in a SBL is $z = \overline{z}$. The energy input given by the horizontal heterogeneous cooling rates can't lead directly to KE development but first has to work against the potential energy stored in the vertical stratification of the virtual potential temperature.

Concerning the divergence pattern of the main circulation, it is found to be significant at the surface. While sinking, the air parcels in the central area, where the perturbation is at its peak, converge between $z = 5m$ and $z = 15m$. As result, the air is laterally advected in this region. To mark is the horizontal structure of the divergence field, which follows from the horizontal structure of the mean circulation (i.e. in the downward branch of the main circulation, between $x = 100m$ and $x = 200m$, the divergence field is almost horizontally homogeneous. Then, going towards $x = 0$ and $x = L$, it disappears following the vertical velocity disappearing). Moreover, wave-like signals are still present

in the vertical divergence field, probably due to the IGWs which were not ruled out by the time mean ($\alpha > 70°$).

IGW dynamic. Internal gravity waves are present in the simulations because the boundary layer is initialized as stable. Moreover, the grid size and the time resolution allow to resolve them. Considering the velocity field and the divergence field shown in [Fig.13], several features can be noticed: the velocity magnitude of the IGWs is one order smaller than the velocity magnitude of the main circulation, but the magnitude of the vertical divergence is the same. The pattern of the vertical divergence field below $z = 30m$ suggests the presence of slanted IGWs there. The pattern seems to repeat itself in the horizontal direction, as it is expected from waves. An IGW, once that time is fixed, is characterized by its propagating vector $\vec{k}$, and even if the phase is dependent on the position, if the horizontal wavelength is smaller than the domain size, the pattern will repeat in the horizontal direction and fill the whole length.

Energy evolution. The dynamic evolution of the system can be divided into two parts. In the first one, dynamic development follows the known theories of stable boundary layers: stratification suppresses kinetic energy [**7**]. The variability of the kinetic energy in the first half-hour suggests the dynamic be at least partially IGW induced, being the frequency proportional to the stratification [**8**]. Internal gravity waves are produced by the horizontal heterogeneity of the cooling rates, which were found to be relevant only inside the perturbation ($z < 125m$). This explains why the magnitude of the kinetic energy is smaller in the region above the perturbation [**6**]; as we said 10% of the total HH is found in the upper part of the domain, thus, the kinetic energy found in the upper region is either produced by this low HH or is a result of upward propagating waves generated in the perturbation. In both cases, the upper part should present smaller values of kinetic energy compared with the lower part. Confronting the magnitude of the surface kinetic energy with the bulk kinetic energy, still, in the first half-hour, the two of them are similar, because HH is almost the same for all levels where the perturbation is prescribed. However, the non-slip conditions at the surface mark a little deficit of kinetic energy at the surface compared with the bulk of the simulation [**6**]. Concerning the perturbation amplitude, result [**9**] shows that there's no linear relation between q'_v and the kinetic energy development, even if a positive correlation exists (i.e. doubling the perturbation amplitude, the kinetic energy development does not double, but it increases of one order). After $t \approx 1h$, the kinetic energy increases considerably everywhere. The increase seems to be triggered from the surface because the kinetic energy there is the first to rise, followed by the bulk kinetic energy and the kinetic energy above the perturbation [**3**]. The rapid insurgence [**2**] suggests an instability behind it. If instability is present and is the reason for the rise of the kinetic energies, the fact that the surface kinetic energy is the first to arise suggests the instability to develop there. This may explain [**1**]: once that the instability is met, bound solutions are not possible anymore and the velocities increase of several orders at the surface. Indeed, the TKE, defined as $\frac{1}{2}\langle u'u'\rangle + \frac{1}{2}\langle v'v'\rangle + \frac{1}{2}\langle w'w'\rangle$ is found

to be, at the surface, on the same order of the KE at the surface, meaning that the surface kinetic energy is for the most part turbulent kinetic energy. The instability seems to be connected with the perturbation amplitude **[4]**, but the kinetic energies at later times are independent by the initial parameters **[5]** and for that, no explanation is provided. If energy is extracted from the vertical stratification following an instability, then it should be expected the kinetic energy at later times to be higher in the simulations with higher stratification values. On the other hand, stratification (still present in the bulk after the instability at the surface develops) suppresses vertical motion, putting these two tendencies in contraposition. However, it is hard to believe the two tendencies to efface each other, and thus no explanation is provided for the kinetic energy's independence on the initial parameters, for later times.
Since the total kinetic energy found in the system is close to being equal to the kinetic energy found at the surface (the other regions have a smaller contribution), **[10]** confirms the existence of a relationship between the variable HH and the time derivative of the total kinetic energy of the system. The kinetic energy above the perturbation is not triggered by the horizontal heterogeneity of the cooling rates, as **[11]** shows, or at least not directly (maybe $\partial_t KE_{other}(t+t')$ and $HH(t)$ are correlated for some $t' > 0$ which will be the characteristic time for a vertical energy propagating process to reach the region $z > 125m$). The time derivative of the kinetic energy in the bulk is correlated with $HH(t)$ only for high stratified layers **[12]** and for this, no explanation is provided. In general, [Fig.16] suggests that the energy input due to the horizontal heterogeneity of the cooling rates ends up triggering motion at the surface.

5.4 Turbulence development

Turbulent vertical fluxes of virtual potential temperature quantify the vertical transport of θ_v by means of vertical velocity fluctuations. In the DALES model, two different turbulent vertical fluxes of θ_v can be identified. The first turbulent vertical fluxes of virtual potential temperature are an analysis of the resolved vertical velocity field and the resolved field θ_v, using the Reynolds decomposition and identified by $\langle w'\theta_v' \rangle$. These turbulent vertical fluxes of virtual potential temperature detect IGWs if the resolution is high enough, as this work asks. The second turbulent vertical fluxes of virtual potential temperature are the SFS-θ_v vertical fluxes defined in [eq.26] with $j = 3$ and parametrized in [Section 2.2] as the vertical gradient of the resolved field θ_v multiplied by $-K_H$. These sub-grid turbulent vertical fluxes of θ_v play a major role in [eq.34]. The latter equation affects then the resolved flow through [eq.31], [eq.29] and [eq.24]. These sub-grid turbulent vertical fluxes of θ_v play a major role also in [eq.23], affecting the resolved field of virtual potential temperature. These two turbulent vertical fluxes of virtual potential temperature are the only ones treated in this section. Moreover, they are studied through their horizontal means, provided as output by DALES. Due to the length of these names, in this section, the name *resolved fluxes* will be used when talking about $\overline{\langle \theta' w' \rangle}$ and the name *sub-grid fluxes* will be used when talking about the $\overline{\text{SFS-}\theta_v}$ vertical fluxes. Their sum will be called

total fluxes.

The resolution of the simulations ($2.34m \times 2.34m \times 2.5m$) should ensure the sub-grid fluxes to be negligible compared to the resolved fluxes and this is almost the case. It is not the case at the surface. This section is divided into three parts. In the first part, the general picture of the fluxes is given. In the second part, the insurgence of the instability $N^2 < 0$ is shown. In the third part, surface fluxes profiles at earlier times are studied. The results shown in this section are from S1 of [Table1]. The results of the other simulations of [Table1] are not shown.

Turbulent fluxes: the general picture

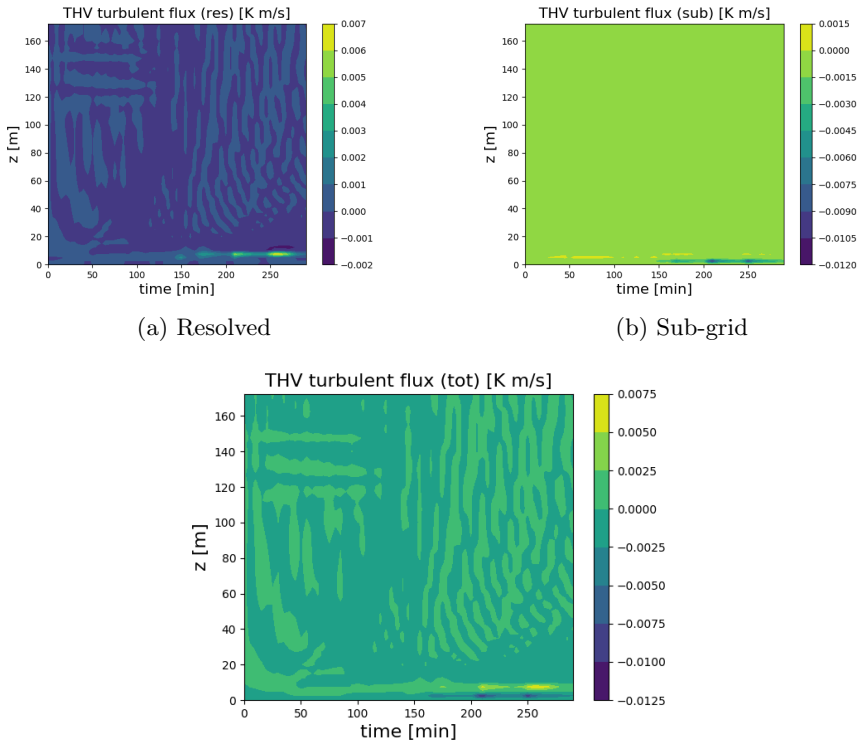

(a) Resolved

(b) Sub-grid

(c) Total

Figure 17: Time series of the resolved, sub-grid, and total fluxes. The domain can be separated into two regions: bulk ($z > 25m$) characterized by low magnitude fluxes and surface ($z < 25m$) characterized by high magnitude fluxes. The resolved fluxes for $z > 25m$ are positive and negative with amplitude $\approx 10^{-8}\ K\ m\ s^{-1}$. The sub-grid fluxes for $z > 25m$ present a negative plateau value of $\approx -10^{-9} K\ m\ s^{-1}$.

In [Fig.17] is plotted the time series of the resolved, sub-grid, and total fluxes. **[1A]** For $z > 25m$, the resolved fluxes present positive and negative values that result in patterns. **[2A]** The patterns in the resolved fluxes penetrate the region above the perturbation. **[3A]** The patterns in the resolved fluxes present a period larger than the natural period of the system ($T = 2\pi/N = 543s$). **[4A]** The patterns in the resolved fluxes present different orientations. **[5A]** For $z > 25m$, the sub-grid fluxes are negative. **[6A]** For $z > 25m$, the variations of the resolved fluxes overcome the negative plateau of the sub-grid fluxes. **[7A]** At the surface, all the fluxes increase.

Surface Instability: $N^2 < 0$

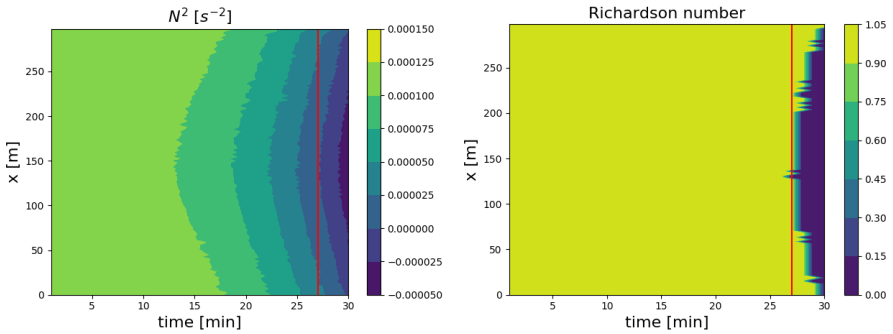

Figure 18: Left. Time series of the Brunt-Vaisala frequency (power two) computed across the line $(y_0, z_0) = (150m, 2.5m)$. Right. Time series of the Richardson number computed across the line $(y_0, z_0) = (150m, 2.5m)$. The red lines correspond to the first time in which a zero value is found.

To understand the surface fluxes, whose magnitudes suggest to be triggered by instabilities, the time series of the Brunt-Vaisala frequency (power two) and the Richardson number are computed across the line $(y_0, z_0) = (150m, 2.5m)$. The vertical gradient of the virtual potential temperature ($\partial_z \theta_v$) and the vertical gradient of the horizontal component of the velocity field ($\partial_z(u^2 + v^2)$) were calculated with a grid gradient (i.e. taking into account values at one level and values at one level above). The Richardson number at $t = 0$ is not definable, being the domain initialized as shear-free, thus R_i is set to 1 anytime that is found above such threshold. Results are shown in [Fig.18]. **[1B]** The power two of the Brunt-Vaisala frequency, which at $t = 0$ is homogeneous in the domain and equal to $1.34 \cdot 10^{-4}\ s^{-2}$, starts decreasing. **[2B]** The break (i.e. $N^2 < 0$) is met at $t = 27\ min$. **[3B]** The Richardson number stays above 1 up to $t = 26\ min$ and suddenly drops to zero at $t = 27\ min$ following N^2.

Turbulent fluxes: surface earlier times

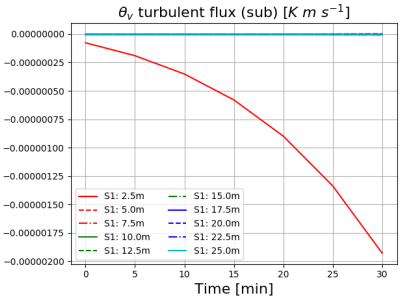

(a) Sub-grid

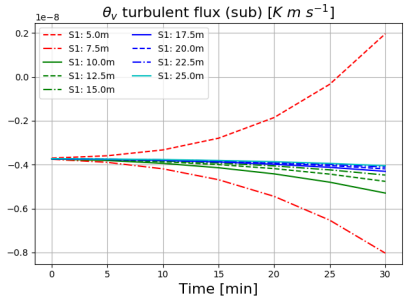

(b) Sub-grid

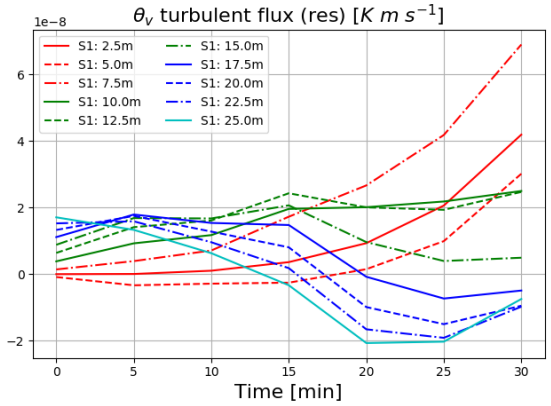

(c) Resolved

Figure 19: Time series of the sub-grid and resolved fluxes for different levels at the surface and in the earlier times of the simulation. In (b), level $z = 2.5m$ is taken out.

To understand the initial vertical structure of the fluxes, not clear in [Fig.17], [Fig.18] shows the sub-grid and resolved fluxes time evolution in the first half an hour and for the levels belonging to the surface. **[1C]** The sub-grid fluxes at $z = 2.5m$ are dominant. **[2C]** The sub-grid fluxes at $z = 5.0m$ become positive at $t = 27min$. **[3C]** The resolved fluxes are positive at the surface up to $z = 15.0m$. **[4C]** The resolved fluxes, above $z = 15.0m$, merge with the patterns found in [1A].

Discussion

- The patterns marked in **[1A]** are the result of IGWs activity. The horizontal heterogeneity of the cooling rates is the trigger for the IGWs to develop. After the initialization, a perturbation $\theta'_v < 0$ is induced in the central region, and $\theta'_v > 0$ is induced in the lateral region. The isolines of θ_v are modified and

IGWs develop to restore horizontal homogeneous isolines, leading to $w' < 0$ where $\theta'_v < 0$ and $w' > 0$ where $\theta'_v > 0$. One, however, can argue that $w' < 0$ where $\theta'_v < 0$ and $w' > 0$ where $\theta'_v > 0$ are results of the main circulation, induced by the cooling rates, and developing after the initialization. He would not be wrong. The point is that IGWs, once produced, do not couple with the perturbations induced by the cooling rates. Let's explain this with math. If IGWs and horizontal heterogeneous cooling rates are present, they both induce fluctuations in θ_v and w. The fluctuations induced by the cooling rates are diabatic, the fluctuations induced by the IGWs are adiabatic[5]. It can be written:

$$\overline{\langle w'\theta'_v\rangle} = \overline{\langle (w'_{CR} + w'_{IGW})(\theta'_{vCR} + \theta'_{vIGW})\rangle} =$$
$$= \overline{\langle w'_{CR}\theta'_{vCR}\rangle} + \overline{\langle w'_{IWG}\theta'_{vCR}\rangle} + \overline{\langle w'_{CR}\theta'_{vIGW}\rangle} + \overline{\langle w'_{IGW}\theta'_{vIGW}\rangle}$$

where the index CR refers to the cooling rates fluctuations, the index IGW to the IGWs fluctuations. Then, assuming the absolute value of w'_{CR} to be equal to the absolute value of w'_{IGW}, the absolute value of θ'_{vCR} to be equal to the absolute value of θ'_{vIWG}, condition that follows from the idea that IGWs are induced by the cooling rates, assuming that the turbulent analysis preserves the IGWs signal (they have a period larger than $10min$) and knowing that the fluctuations θ'_{vIWG} and w'_{IWG} are out of phase, it can be written:

$$\begin{aligned}\overline{\langle w'\theta'_v\rangle} &= \overline{\langle w'_{CR}\theta'_{vCR}\rangle}(1 + \sin(\omega_I t) + \cos(\omega_I t) + \sin(\omega_I t)\cos(\omega_I t)) \\ &= \overline{\langle w'_{CR}\theta'_{vCR}\rangle}(1 + \sqrt{2}\sin(\omega_I t + \frac{\pi}{4}) + \sin(\omega_I t)\cos(\omega_I t))\end{aligned} \tag{43}$$

where ω_I is the frequency of the IWGs, t is time and $\overline{\langle w'_{CR}\theta'_{vCR}\rangle} > 0$ for the reasons given at the beginning. Even if this formula presents many simplifications, it states that the time series of the resolved fluxes should be an oscillating function presenting positive and negative values, starting as a sine function at phase $\pi/4$ with a positive value. From [Fig.19-C], this seems the case for $z > 15m$ and it is up to $z = 50m$ ([**4C**]). The equation holds at these levels because the cooling rates are close to being vertical homogeneous there. Vertical homogeneous cooling rates result in the production of only horizontal propagating internal gravity waves (thus, one frequency). On the other hand, above $z > 50m$, the cooling rates present a non-negligible vertical structure that produced slanted IGWs with a different frequency. In other words, the biggest simplification in [eq.43] is that the IGWs present just one frequency, while actually, as it is shown in [Section 5] there are two.

- Results [2A], [3A], and [4A] confirm what was shown in point [1A]. The penetration of the patterns in the region above the perturbation ([**2A**]) is explainable only with a vertical transport of energy because the HH above the

[5]This is the main difference between the two. The fluctuations induced by the cooling rates are permanent, energy is extracted from the air parcel that sinks to lower potential energy levels. The fluctuations induced by IGWs are an exchange between kinetic and potential energy, preserving the air parcel total energy.

perturbation was found to be negligible ([Fig.9]). Thus, the energy cannot be ascribed to the HH above the perturbation but it must be transported from below. Result **[3A]** follows from the fact that the frequency of the patterns, according to [eq.43], is due to IGWs and these cannot have a frequency higher than the Brunt-Vaisala frequency. Result **[4A]** shows the presence of slanted waves, which are generated by the vertical structure of the cooling rates and are proven to be in [Section 5].

- The sub-grid fluxes for $z > 25m$ are negative (**[5A]**) because the vertical stratification is never broken in the bulk, and thus $-K_H \partial_z \theta_v$ is negative for all times. The resolved fluxes at $z > 25m$ can overcome such negative plateau (**[6A]**), meaning that the IGWs have the potential to destroy the stratification. In lower resolution simulations, the IGWs will not be resolved (thus, no oscillations in the resolved fluxes) but it is not known if the positive contribution of the cooling rates (i.e. $\overline{\langle w'_{CR} \theta'_{vCR} \rangle} > 0$) would still overcome the negative plateau of the sub-grid fluxes. Most likely yes, and it will be the reason for the formation of a circulation.

- The break of the stratification cannot be ascribed to the shear-instability because the Richardson number does not decrease, but suddenly drops to zero following the Brunt-Vaisala frequency drop, as pointed out in **[3B]**; for instance, at $t = 25min$, the power two Brunt-Vaisala frequency is $5 \cdot 10^{-5} s^{-2}$ and the Richardson number is still above 1, meaning that the vertical shear of the horizontal velocity, also called Prandtl frequency, is $\approx 7 \cdot 10^{-3} s^{-1}$ and should not be to able to break the vertical stratification. Nevertheless the break occurs at $t = 27min$, as stated in [**2B**] and observed even in the sub-grid fluxes ([**2C**]).

- The process behind the instability may then be the advective instability. Result [**3C**] seems to point in this direction. From [eq.43] the combined effect of the cooling rates and the IGWs can be seen under this light: the horizontal heterogeneous cooling rates tends to increase $\langle w' \theta'_v \rangle$ towards positive values, the IWGs counter this tendency reestablishing the stratification (i.e. the IGWs tend to reestablish the horizontal isolines of θ_v). For inertia, the counter effect becomes a positive feedback, leading to the maximum positive peaks. If the non-linear effects are present, then they occur in the phase where there's a positive feedback (i.e. when the wave is deforming the isoline of virtual potential temperature the most). The reestablishment of the isolines of θ_v is then not completed because the wave is partially destroyed. This mechanism, perhaps happening at the surface, would leave localized $\theta'_v < 0$ from the lower levels in the higher levels, up to $z = 15m$, and localized $\theta'_v > 0$ from the higher levels in the lower levels, explaining the positive resolved fluxes at these heights (**[3C]**). This will be an explanation also for the decrease of stratification seen in **[1B]**. Given that the air between $z = 0m$ and $z = 15m$ is mixing, the rise of negative sub-grid fluxes at the surface, which is seen only at $z = 2.5m$, is a result of the cold surface at contact with warmer air coming from the upper layers (**[1C]**-**[7A]**).

- However, another explanation for the last results (results with index **B**,**C** and [**7A**]), is a mistake in the implementation of the surface conditions. The resolved fluxes at $z = 0$ are zero because $w = 0$ there, while the sub-grid fluxes at $z = 0$ are prescribed to be zero. Then, the vertical gradient of the sub-grid fluxes, which is a source in [eq.23], will be a positive source in the first level, increasing the temperature there and leading to instabilities. This underlines the turbulent insurgence to be a result of a mistake, rather than a real process. Due to lack of time, simulations prescribing negative values of sub-grid fluxes at the surface were not carried (in particular, from [Fig.19-A], the surface sub-grid fluxes should be prescribed with value $-2.5 \cdot 10^{-7} Kms^{-}1$).

5.5 Fourier analysis of the wave-like signals

To get a better insight over the wave-like signals observed in the simulations, a Fast Fourier Transformation (FFT) can be applied over the velocity field. The FFT can be applied at fixed positions, to find the frequencies explaining the velocity field variations, or at fixed times, to find the wavelengths explaining the velocity field spatial distribution. However, while the FFT at fixed positions shows clearly the presence of two major frequencies in the frequency spectrum, the FFT at fixed times shows no such consistency in the wavelengths spectrum, and no preferred wavelengths were found. This is a drawback, because through the wavelengths, the condition for non-linearities to be relevant (a condition needed for the occurrence of the advective instability), readily [eq.19], could have been checked.

Frequency spectrum vertical profile

Among the three components of the velocity field, the vertical component was selected for the FFT analysis. This choice was motivated by the vertical anisotropy of the NSBL. The vertical velocity time series, spanning the first hour and in the column $(x_0, y_0) = (L/2, L/2)$, were selected. The focus is on the first hour because the first instability develops in that time window. The focus is on the vertical column $(x_0, y_0) = (L/2, L/2)$ to understand which frequencies are present at a certain height. Given these 128 time series (one for each vertical level) a FFT over time is applied to each of them. The two most probable frequencies found in a level are then selected. In the lowest levels, the high variability of the velocity field, which follows the instability, leads to frequencies above the Brunt-Vaisala. For plot reasons, frequencies above the Brunt-Vaisala are set to zero.

In [Fig.20] are plotted the vertical profiles of the two most probable frequencies (red most probable, blue second most probable) explaining the time variability of the velocity vertical component. The simulation analyzed is S1. [**1**] Zero values of frequency are found at the surface ($z < 25m$). [**2**] In the bulk ($z > 25m$), the most probable frequencies are below N and non zero. [**3**] For $z > 75m$ the most probable frequency is higher than the second most probable, or they are

the same. [**4**] For $25m < z < 75m$ the most probable frequency is almost ever smaller than the second most probable.

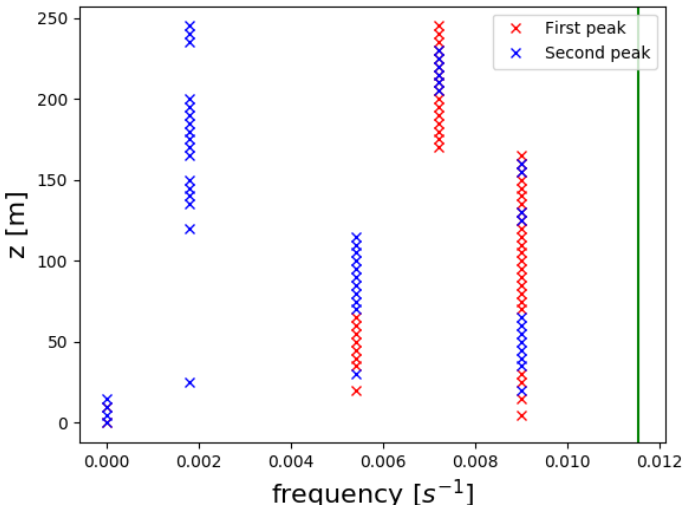

Figure 20: Vertical profiles of the two most probable frequencies (red most probable, blue second most probable) found through a FFT of the velocity field vertical component applied at each point of the column $(x_0, y_0) = (L/2, L/2)$ in the first hour of the simulation. The green line corresponds to the Brunt-Vaisala frequency of the system at $t = 0$. Results are from S1.

Discussion

- Result [**1**] follows from the instability found at the surface: the instability locally breaks the stratification, leading to locally unbounded solutions. As result, the frequency spectrum loses its coherence at the surface, presenting amplitudes for all frequencies.
- Result [**2**] confirms the nature of the wave-like signals. In the bulk of the simulation ($z > 25m$) the stratification is never destroyed, thus, short-period variations of the vertical velocity field are not found. On the other hand, the two most probable frequencies are found to follow the internal gravity wave theory, being both below N. The two frequencies can be associated with two IGWs, propagating at two different angles. Frequencies and propagating directions are connected through [eq.16], neglecting the inertial contribution: $\nu_1 = N\cos(\alpha_1)$ and $\nu_2 = N\cos(\alpha_2)$. The consistency of the frequencies vertical profiles supports this idea as well because it is not expected a wave to drastically change its frequency across layers, especially in a system initialized with a homogeneous stratification. A discontinuity is present only at $z = 125m$. This height marks

the end of the imposed perturbation and the discontinuity is most likely to be attributed to that aspect. Assuming this insight right, the higher frequency can be associated with more horizontal propagating IGWs, the lower frequency with more slanted propagating IGWs.
- Results [**3**] and [**4**] state that in the upper part of the domain ($z > 75m$), the horizontal IGWs are dominant, while in the lower part of the domain ($z < 75m$), the slanted waves are dominant. This can be the reason for the surface instability to rise; slanted waves, breaking at the surface, have the potential to achieve the condition for non-linearities [eq.19], and thus leading to advective instability. Indeed, increasing the propagation angle and keeping the amplitude of the wave constant, the horizontal component of the velocity field associated with the wave increases (U in the non-linearities criterion). This process could be similar to horizontally propagating IGWs, induced by large scale conditions, which break when the land surface tilts. In the current case, the horizontal heterogeneity of the cooling rates, induced by a perturbation of water vapor with an aspect ratio close to one, produce slanted IGWs that breaks at the flat surface.

6 Conclusions

The goal of the thesis, showing that turbulence production is possible even in the shearing stable NSBL, is partially achieved in the DALES model because it can be a result of a bad implementation of the surface conditions. Out of the results shown, three hypotheses, explaining the turbulent production, can be advanced.

The first physical hypothesis is that horizontal heterogeneous conditions of specific humidity not only may sustain a circulation but producing internal gravity waves, are also able to mechanically destroy the stratification close to the surface and lead to turbulence production. This turbulence, being mechanically induced and not shear-induced, is independent of the Richardson number. This conclusion underlines that IGWs, not considered in large scale models, can be the explanation for the underestimation of turbulence in these models.
The second possible conclusion is for this work to have overestimated the energies carried by the IGWs. Indeed, the periodic boundary conditions implemented by DALES do not fit the study for propagating energy signals. Waves should be able to propagate in the horizontal direction and leave the system. This is not possible in the DALES model, where the dynamic conditions at $x = 0m$ are set to be equal to the dynamic conditions at $x = L$. However, even if this may be true, the first hypothesis will still hold, but for a series of perturbations rather than a single one.
The third possible conclusion is that the advective instability, which we were not able to prove, does not take place at all. In this case, the surface instability is not due to the shear of the flow, neither to the displacement induced by buoyancy waves. Still, the instability and the mixing at the surface are present, and this underlines another form of instability, different from the shear-instability and the advective instability. This may also be a result of wrong conditions at

the surface.

Future works should firstly implement better conditions at the surface. If the surface mixing is still observed, the focus should be on resolving the wavelengths of the wave-like signals, to assess if the criterion for non-linearities is met. This will erase the possibility for the third conclusion. Secondly, high-resolution in-field measurements of the specific humidity field should be taken in shearing stable NSBL presenting turbulent transport. If the horizontal heterogeneity of the specific humidity field is found to be relevant, then most likely the observed turbulent transport is due to the first hypothesis also in the real world scenario. Numerical schemes are deeply flawed by not being the real world, and results from them should never be trusted over in-field measurements. If these two points are verified, a new mechanism would have been discovered. Starting from that, parametrization of IGWs turbulence induced by horizontal heterogeneous specific humidity values should be the next step to improve the computation of turbulence in large scale models. A parametrization should be sought connecting the small scale variations of the specific humidity field with larger, resolved, phenomena. Another parametrization should then be sought connecting the small scale variations of the specific humidity field with the turbulent production at the surface. In this way, from resolved phenomena connected with the formation of horizontal heterogeneous water concentrations, a better estimate of turbulence in the NSBL can be given.

References

André, J., & Mahrt, L. (1982). The nocturnal surface inversion and influence of clear-air radiative cooling. *Journal of the Atmospheric Sciences*, *39*(4), 864–878.

Carlson, M. A., & Stull, R. B. (1986). Subsidence in the nocturnal boundary layer. *Journal of climate and Applied Meteorology*, *25*(8), 1088–1099.

Cuxart, J., Holtslag, A. A., Beare, R. J., Bazile, E., Beljaars, A., Cheng, A., ... others (2006). Single-column model intercomparison for a stably stratified atmospheric boundary layer. *Boundary-Layer Meteorology*, *118*(2), 273–303.

de Roode, S. R., Bosveld, F. C., & Kroon, P. S. (2010). Dew formation, eddy-correlation latent heat fluxes, and the surface energy imbalance at cabauw during stable conditions. *Boundary-layer meteorology*, *135*(3), 369–383.

Fu, Q., & Liou, K. (1992). On the correlated k-distribution method for radiative transfer in nonhomogeneous atmospheres. *Journal of the Atmospheric Sciences*, *49*(22), 2139–2156.

Heus, T., van Heerwaarden, C., Jonker, H., Siebesma, A. P., Axelsen, S., van den Dries, K., ... others (2010). Formulation of and numerical studies with the dutch atmospheric large-eddy simulation (dales). *Geosci. Model Dev*, *3*, 415–444.

Hohenegger, C., & Stevens, B. (2016). Coupled radiative convective equilibrium simulations with explicit and parameterized convection. *Journal of Advances in Modeling Earth Systems*, *8*(3), 1468–1482.

Jacobitz, F. G., Rogers, M. M., & Ferziger, J. H. (2005). Waves in stably stratified turbulent flow. *Journal of Turbulence*(6), N32.

Kataoka, T., & Akylas, T. (2015). On three-dimensional internal gravity wave beams and induced large-scale mean flows. *Journal of Fluid Mechanics*, *769*, 621.

Koop, C. G., & Browand, F. (1979). Instability and turbulence in a stratified fluid with shear. *Journal of Fluid Mechanics*, *93*(1), 135–159.

Naumann, A. K., Stevens, B., Hohenegger, C., & Mellado, J. P. (2017). A conceptual model of a shallow circulation induced by prescribed low-level radiative cooling. *Journal of the Atmospheric Sciences*, *74*(10), 3129–3144.

Newsom, R. K., & Banta, R. M. (2003). Shear-flow instability in the stable nocturnal boundary layer as observed by doppler lidar during cases-99. *Journal of the atmospheric sciences*, *60*(1), 16–33.

Ohya, Y., Neff, D. E., & Meroney, R. N. (1997). Turbulence structure in a stratified boundary layer under stable conditions. *Boundary-Layer Meteorology*, *83*(1), 139–162.

Staquet, C., & Sommeria, J. (2002). Internal gravity waves: from instabilities to turbulence. *Annual Review of Fluid Mechanics*, *34*(1), 559–593.

Sun, J., Burns, S. P., Delany, A. C., Oncley, S. P., Horst, T. W., & Lenschow, D. H. (2003). Heat balance in the nocturnal boundary layer during cases-99. *Journal of Applied Meteorology*, *42*(11), 1649–1666.

Zilitinkevich, S., Elperin, T., Kleeorin, N., & Rogachevskii, I. (2007). Energy- and flux-budget (efb) turbulence closure model for stably stratified flows. part i: steady-state, homogeneous regimes. In *Atmospheric boundary layers* (pp. 11–35). Springer.